Marine and Petroleum Geology
December 2024, Volume 170, Pages 107088 (25p.)
https://doi.org/10.1016/j.marpetgeo.2024.107088 https://archimer.ifremer.fr/doc/00908/101947/

Did gas-hydrate dissociation promote slope instability in the western Black Sea after the end of the last glacial period?

Fabre Maud [1, 2, *], Loncke Lies [2], Riboulot Vincent [1], Ker Stephan [1]

[1] Ifremer, UMR6538 Geo-Ocean, F-29280 Plouzané, France
[2] Université de Perpignan Via Domitia , CEFREM, Perpignan, France

* Corresponding author : Maud Fabre

Abstract :

Submarine landslides constitute major marine and coastal geohazards, causing damage to marine infrastructures or even provoking tsunamis. For many authors, gas hydrate dissociation represents an effective triggering mechanism in generating sedimentary instabilities. In the Romanian upper slope of the Black Sea, failure headscarps are observed in an active gas-seep province close to the gas hydrate occurrence zone acting as an effective seal preventing gas from reaching the seafloor (Popescu et al., 2007; Riboulot et al., 2017). Through a chronostratigraphic interpretation of a large multi-resolution geophysical database, the aim of this article is, for a key period extending from the last glacial period (ca. 33.5-17 ka BP) to the present day, to test the claim of a sudden and instantaneous scenario developed by Kennett et al. (2003), which argue that hydrate dissociation can trigger large-scale landslides on submarine continental margins. Our results show that pronounced gas hydrate dissociation in the Black Sea in response to rapid environmental changes since the last glacial period (Riboulot et al., 2018), does not appear to be the exclusive and main triggering factor of the observed slope failures. This statement is supported by new dating of successive failure events put forward in this study, and the fact that the current and past modelled free gas and hydrate interfaces are much deeper than the basal shear surfaces of instabilities. Alternatively, we suggest that high sedimentation rates, falling hydrostatic pressure, and gas exsolution linked to rapid sea-level lowering are probably the most significant preconditioning factors to consider. Seismic activity cannot be ruled out, given the proximity of active faults on the outer shelf.

HIGHLIGHTS

► Three surficial failure stages since the end of the last glacial period ►Landslides all initiated in the free-gas domain outside the hydrate zone ► The role of hydrate dissociation on recent failure stages is not suspected ► Fluid overpressure, sediment overload, canyon incision and tectonics are probable factors involved in slope instabilities

Keywords : Slope instability, fluid overpressure, gas hydrates, geohazards, western Black Sea, Last Glacial Period.

1. INTRODUCTION

Submarine slope failures redistribute large volumes of sediments from the shelf or the upper slope to the deep basin. They constitute a major threat to the coastal population (Maslin et al., 2010; Paull et al., 2011) and marine infrastructures (Locat and Lee, 2002; Schnyder et al., 2016; Zander et al., 2018). Consequently, increased effort has been invested over the last few decades to understand the timing and mechanisms controlling submarine landslides (e.g. Riboulot et al., 2013; Urlaub et al., 2013). Preconditioning factors and triggering mechanisms on continental margins strongly differ according to site-specific settings (Vanneste et al., 2014).

In this context, the question of the effect of Gas Hydrate (GH) dissociation on slope stability remains debated. Some authors suggest that dissociation of GH leads to a loss of sediment cohesion and excess pressure that is highly conducive to sediment failure (e.g. McIver, 1982; Kvenvolden, 1993, 1994,1996; Paull et al., 1996; Pauli et al.,2003 ; Nixon et al., 2007 ; Nian et al., 2020 ; Nisbet and Piper, 1998; Bouriak et al., 2000; Mountjoy et al., 2014). Other authors, based on numerical modelling, highlight the fact that hydrate dissociation is a slow process rather than an instantaneous and rapid event, where excess pore-pressure generation and recrystallization of hydrates, preferentially at the base of the Gas Hydrate Stability Zone (GHSZ), play a self-controlling role in hydrate dissociation progression and prevent instability (Sultan, 2007; Colin et al., 2020b). Sultan (2007) shows that the top of the GH occurrence zone is significantly more hazardous than its bottom due to the hydrate dissolution process generating overpressure and reducing sediment strength. The relationship between hydrate destabilisation and slope instability is of foremost importance since, governed by temperature-pressure changes, GH are currently undergoing dissociation in many margins of the world (Mienert et al., 2005; Westbrook et al., 2009; Ferré et al., 2012; Phrampus and Hornbach, 2012; Ketzer et al., 2020; Ruppel and Kessler, 2017; Li et al., 2017; Minshull et al., 2020; Davies et al., 2021)

The Black Sea is recognized as a site of active free-gas seepage from the sediment into the sea, with the presence and dissociation of GH (Naudts et al., 2006; Riboulot et al., 2017; 2018; Riedel et al., 2021; Vassilev and Dimitrov, 2002; Popescu et al., 2007; Haeckel et al., 2015; Zander et al., 2017; Hillman et al., 2018a). The successive environmental changes that have taken place since the end of the Last Glacial Period (LGP) in the Black Sea have led the hydrate system to evolve spatially through time (Popescu et al., 2006), particularly in response to sea-level fluctuations and temperature warming (Constantinescu et al., 2015; Soulet et al., 2010). The recent work of Riboulot et al. (2018), based on numerical modelling, highlights the fact that the gas-hydrate dissociation is still in progress due to sediment re-salinisation of the Black Sea that began 9,000 years ago with the reconnection of the Black Sea with the Mediterranean Sea.

Multiple head scarps and remobilized sediments are observed in the northern sector of the Danube-Viteaz Canyon, especially on the upper slope between the shelf break at 190 m and 900 m water depths (Riboulot et al., 2017), mainly above the upper limit of the current GHSZ at around 660 m water depth (Vassilev and Dimitrov, 2002; Popescu et al., 2007; Haeckel et al., 2015; Riboulot et al., 2017; Zander et al., 2017; Hillman et al., 2018a; Marsset et al., 2022). The presence of failure processes and the unique aspect of the Black Sea during deglaciation make it an appropriate site to test the hypothesis of hydrate dissociation causing slope instability during deglaciation. To this end, we have (1) conducted detailed mapping of recent landslides using a very comprehensive set of bathymetry and multi-resolution seismic data (GHASS and GHASS2 campaigns, //doi.org/10.17600/15000500 and //doi.org/10.17600/18001358 respectively), (2) published chronostratigraphic models (Ross and Degens, 1974; Major et al., 2002; Bahr et al., 2005; Soulet et al., 2011a; Constantinescu et al., 2015; Martinez Lamas et al., 2020) to constrain the age of the identified landslides (3) used numerical models of GH stability evolution since the end of the LGP published by Fabre et al. (2024), tested the role of hydrate dynamics on submarine landslide triggering.

2. GEOLOGICAL AND OCEANOGRAPHIC SETTING, PREVIOUS WORK

2.1. Geological setting of the western Black Sea

The western Black Sea is a semi-isolated basin **(Fig. 1b)**, which formed in the Early to Late Cretaceous in a back-arc basin, in association with the northward subduction of the Tethyan Plate (Robinson, 1997; Nikishin et al., 2003). The back-arc opening of the Black Sea is marked by a major southwest-northeast extensional episode resulting in large crustal Mesozoic structures. This extension led to the formation of isolated block systems in horsts and grabens in the north-western zone on the present-day Romanian continental shelf (Dinu et al., 2005; Munteanu et al., 2011; Anton et al., 2019). At the end of the Eocene, the southward collision between the main tectonic units (Pontides and Taurides), led to a tectonic inversion of all the extensional fault systems formed during the Cretaceous (Dinu et al., 2002).

From the early Miocene, the Black Sea acted as a large sediment catchment area, which accumulated a sedimentary sequence 11 km to 19 km thick in its eastern and western basins respectively (Nikishin et al., 2003). The high sediment load on the outer shelf and upper slope and high subsidence rates led to gravitationally induced stress and thin-skinned tectonics from the shelf to the continental slope (Rowan et al., 2004; Konerding et al., 2010; Dinu et al., 2002, 2003; Matenco et al., 2016), including northeast-southwest normal, reverse, and low-angle faults confined to the upper few kilometres of sediment. The décollement layer of this thin-skinned tectonics is identified within the Oligocene to Lower-Miocene series (Matenco et al., 2016).

During the Plio-Quaternary, sedimentation is controlled by western Black Sea rivers such as the Danube, the Dniepr, Dniester, and Bug (De Leeuw et al. 2018; Nikishin et al., 2003), which supply most of the sedimentary load from Central and Eastern Europe, and formed a 2.5 to 3-km-thick prograding depositional wedge. Its depocenter occupies the 100-km-wide continental whole shelf (<190 m water depth) and the present-day north-western continental slope of the Black Sea **(Fig. 1)** (Winguth et al., 2000; Irina Popescu et al., 2004; Lericolais et al., 2009). Northeast-southwest gravitational normal fault systems reactivated along the shelf break (later reactivated during the Pontian, i.e. Messinian) and were active in the Quaternary (Fig. 1). They produced offsets in the order of a few metres to tens of metres clearly visible on the current sea bottom (Tambrea et al., 2002; Dinu et al., 2002, 2005; Konerding, 2005, 2010; Marsset et al., 2022).

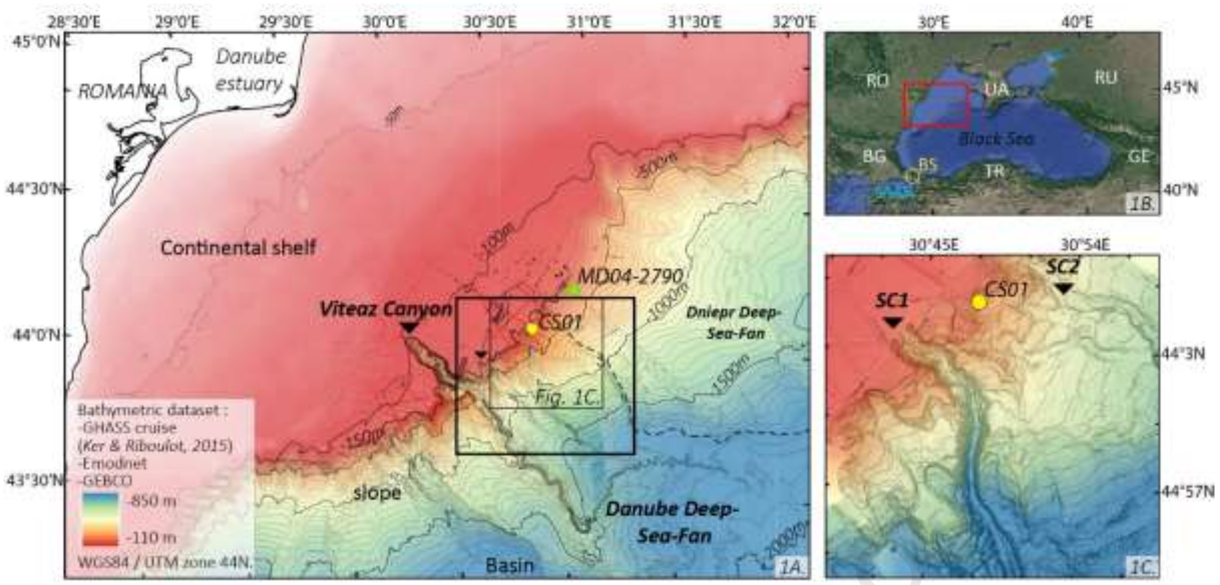

Figure 1:1A.: Location map of the western Romanian margin of the Black Sea; 1B.: General view of the Black Sea: RO for Romania, UA for Ukraine, RU for Russia, GE for Georgia, TR for Turkey, BG for Bulgaria, and BS for Bosphorus Strait. 1C.: Detail on the study area. On Figure 1A., the Danube River, runs into the Black Sea though the Danube estuary, 240 km away from the shelf break and extending seaward to the Viteaz Canyon, deeply incising the outer shelf and the upper continental slope. The modern Danube deep-sea-Fan extends to more than 1500 m water depth. The black frame represents the location of the study area, located to the north of the Viteaz Canyon, in an incised area, which extends from the outer shelf to the middle slope domain at 1500 m water depth. Gravitational normal faults are represented on the outer-shelf, in black lines. 1C.: The close-up shows a bathymetric detail of the study area characterised by the presence of secondary canyons SC1 and SC2, which are highly incised the upper slope. This detail shows also numerous remobilised areas associated with head-scarps. The core CS01 presented in the study is represented with a yellow disc. The core MD04-2790 used for the dating is represented with a green disc.

2.2. Hydrologic and climatic Quaternary evolution of Black Sea

During the Quaternary, the Black Sea oscillated from freshwater lake conditions to an open saltwater marine environment (Deuser 1972), in response to alternating glacial and interglacial periods (Ryan et al., 1997; Poort et al., 2005; Badertscher et al., 2011).

During low eustatic sea-level conditions, i.e. during glacial periods, disconnection with the Sea of Marmara and the Mediterranean Sea, through the Dardanelles and Bosphorus straits (-35 m water depth) (Fig. 1b, BS corresponding to Bosphorus) led to an evolution in sea level in the Black Sea decoupled from global sea-level fluctuations. The last low-stand fresh-water phase in Black-Sea, also known as the Neoeuxinian phase in Black-Sea literature, prevailed during the last glacial cycle, also known as the Last Glacial Period (LGP). The LGP occurred from the end of the Last Interglacial to the beginning of the Holocene, c. 115,000 – c. 11,700 years ago, and thus corresponds to most of the time span of the Late Pleistocene (Corrick et al., 2020). At the end of the LGP, the Last Glacial Maximum (LGM), which took place in the Northern Hemisphere from -26.5 to -19 ka (Clark et al., 2009) is characterised by a maximum amplitude of sea-level fall, has no strict eustatic equivalent in the Black Sea. Thus, in this study, we define the End of the Last Glacial Period (E-LGP) specifically as a lapse of time extending from -34 ka (the minimum age investigated in this study) to the reconnection with the Mediterranean at 9 cal a BP (Soulet et al., 2011a).

Reconstruction of hydrological conditions using geochemical pore-water profiles provides some insights into salinity and bottom water temperatures during this E-LGP with values of ~2 g/L and 4°C (Soulet et al., 2010). The Black Sea water level during the E-LGP was first estimated between ~90-150 m lower than the current one (Deuser 1972; Ryan et al., 1997; Popescu et al., 2004; Lericolais et al., 2011; Constantinescu et al., 2015; Yanchilina et al., 2017).

However, Martinez-Lamas et al. (2020) recorded periods of rising sea level during the E-LGP related to enhanced surface melting of the Alpine Ice Sheet. This consequently resulted in five main periods of increased river-flood frequency (ca. 33.5-15 ka interval), each of 1.5-3 ka duration, synchronous with Heinrich Stadial 3 (HS i.e. a stadial which contains a Heinrich event, Sanchez Goni and Harrison, 2010) (ca. 32-29 ka), Greenland Stadial 4 (ca. 28.6-27.8 ka) and Heinrich Stadial (HS 2) (ca. 26-23.5 ka).

After 15,700 ± 300 cal a. BP, a major sea-level rise ranging between +90 m to +120 m ensued

(Constantinescu et al., 2015), associated with North Hemisphere Ice-sheet melting at the end of the glacial period. This flood event induced reconnection of the Black Sea freshwater with the Mediterranean (Aksu et al., 2002; Hiscott et al., 2007) at 9,000 cal a. BP via the shallow Bosphorus Strait (Soulet et al., 2011b). This reconnection resulted in sea-bottom temperature warming (4°C to 8.9°C) and salinity increase (~2 g/L to ~22 g/L) associated with marine conditions (Soulet et al., 2010; Riboulot et al., 2017).

2.3. The Danube sedimentary system in the Black Sea since the last glacial period

The Danube sedimentary system is dominated by the presence of the Viteaz Canyon **(Fig. 1a)** that developed since -34,000 cal a BP (Martinez-Lamas et al., 2020) and which constitutes the modern offshore continuity of the Danube River, which was already functioning during the period of low-stand conditions of the Black Sea (Popescu et al., 2004). The Viteaz Canyon incised the continental margin over 26 km to 110 m water depth on the outer shelf, and continues as a channel with well-developed lateral levees on the upper slope, beyond the shelf break (Popescu et al., 2004) **(Fig. 1a)**.

Previous studies show that periods of canyon and fan activity were systematically associated with the lacustrine phases of the basin, although this activity was interrupted during marine high-stand phases (Panin 1989, 1997, 2002; Wong et al., 1994; Constantinescu et al., 2015). Effectively, during the E-LGP, sediment supply was associated with hyperpycnal currents or with glacial melting discharge (Popescu et al., 2004; Martinez-Lamas et al., 2020). The sediments were mostly exported downslope though the Viteaz Canyon to the deep domain (Panin, 1989), resulting in a stack of channel-levee complexes ~450 m thick each, and the development of a deep-sea fan between 1500 and 2000 m water depth (*Danube Deep-Sea Fan* in **Fig. 1a)** (Wong et al., 1994; Winguth et al., 2000; Popescu et al., 2001, 2004, 2006; Lericolais et al., 2009, 2011; Lericolais et al., 2013).

Based on a long piston core description from the north-west Black Sea margin (core GAS-CS01), Martinez-Lamas et al. (2020) propose that the latest modern deep-sea fan complex developed after 34,000 cal a BP, during the lowstand lacustrine period, when the Danube River was connected to the Viteaz Canyon mouth **(Fig. 1a).** Through a sedimentological analysis on the upper slope, they show that the associated sediments consist of a succession of coarsening-upward and then fining-upward units characteristic of hyperpycnal turbidity-current deposits (Mulder et al., 2003), providing a high-resolution river flood record in the north-west Black Sea over the ca. 33.5-17 ka interval. Four main periods of enhanced Danube flood frequency, each of 1.5-3 ka duration, are recorded at 32.5-30.5 ka (F5), at 29-27.5 ka (F4), at 25.3-23.8 ka (F3) and at 22.3-19 ka (F2). Similarities in both the stratigraphy and sedimentology observed in core MD04-2790 (Soulet et al., 2011a), in the Dniepr domain, highlight the regional imprint of river floods in the study area.

The sedimentology and dating information used in this study derives from the Calypso long-piston core GAS-CS01 studied by Martinez Lamas et al. (2020). This 32.1-m-long core shows a lithological succession, observed from the western Black Sea upper slope (Bahr et al., 2005; Major et al., 2002; Soulet et al., 2011a) to the Danube deep-sea fan (Constantinescu et al., 2015). From the top down, it consists of marine Unit I (Marine Cocoolith Ooze (MCO), <2720 ± 160 cal a BP) and Unit II (sapropel, deposited from 8,080 ± 250 cal a BP) and then, lacustrine Unit III described by Ross and Degens (1974). In order to more accurately date Unit III, Martinez-Lamas et al. (2020) used two approaches: (1) they correlated GAS-CS01 with core MD04-2790 (location in Figure 1a) (Soulet et al., 2011a) using their extremely similar XRF-Ca records (refer to Supplementary materials *Table 2* in Martinez Lamas et al., 2020). Indeed, the authors considered the robustness of the calendar age-depth model published by Soulet et al. (2011a), that was reconstructed with an alignment approach of TEX86-derived Lake Surface Temperature with the Hulu Cave $\delta^{18}O$ speleothem record (Wang et al., 2001), (2) in depth, the chronology is based on radiocarbon age ^{14}C yr BP (Dreissena sp. and bulk organic matter), bounding back to ~34 ka at the base of the core (refer to Supplementary materials *Table 2* in Martinez Lamas et al., 2020).

Accordingly, core GAS-CS01 contains a very-high-resolution record of the marine and glacial lacustrine Units I, II and III (until ca. 33.5 ka) (Martinez-Lamas et al., 2020).

2.4. The gas-hydrate system of the Black Sea

Limited water-circulation and water-body exchanges between the Black Sea and the Mediterranean via the shallow Bosphorus Strait led to unusually low oxygenation conditions of the water column through time. The highly saline Mediterranean water (38 psu) flows deep into the Black Sea under the freshwater it receives from its watershed (Panin and Jipa, 2002). It results in a very marked stratification of the water column, with low salinity (~18 psu), oxygenated surface waters and anoxic, salty (~22 psu) deep waters (Ozsoy et al., 2002; Bahr et al., 2005; Rank et al., 1999). The Black Sea is currently considered as the largest land-locked anoxic basin in the world (Caspers, 1957, Demaison & Moore, 1980). Consequently, high amounts of organic matter were preserved in deep and surficial sediments and their decomposition and cracking have led to high amounts of both biogenic and thermogenic methane being trapped in sediments (Burwicz & Haeckel, 2020).

Numerous studies have evidenced active gas seepages from the seafloor in the Black Sea. They mainly occur on the upper slope and continental shelf (Dimitrov and Vassilev, 2003). Many fluid escape indicators such as pockmarks, carbonate chimneys, boiling seafloor swamps and mud volcanoes on the seafloor have been described (Dimitrov and Vassilev, 2003; Kruglyakova et al., 2004). More than 10,000 seepage sites over an area of ~ 3000 km² have been identified on the upper slope along the western Black Sea margin (Naudts et al., 2006). Among them, ~ 2000 have been detected in the Romanian sector (Riboulot et al., 2017; Riedel et al., 2021). Free gas mainly escapes along canyon incisions such as canyon SC1 (Figure 2), both along the axial thalweg and canyon flanks, or through slope-failure head-scarps (Popescu et al., 2004; Riboulot et al., 2017, **Fig. 2**). Gas escapes also occur along deep-sea channels and levees deposits (Hillman et al., 2018b; Ker et al., 2019; Riedel et al., 2021) **(Fig. 2)**. It is important to underline that the vast majority of observed active seepages occur outside the current GHSZ **(Fig. 2)** (Riboulot et al., 2017), where GH accumulation acts as an effective seal hampering free gas from reaching the seafloor and the water column.

The GH have been studied and largely mapped on the western Romanian slope of the Black Sea (Popescu et al., 2007; Zander et al., 2017; Riboulot et al., 2017, 2018; Riedel et al., 2021). Seismic data reveal the presence of a bottom-simulating reflector (BSR) imaging the current free gas and GH interface in response to a high impedance contrast in many areas of the Romanian margin (Popescu et al., 2006; Haeckel et al., 2015; Zander et al., 2017; Riboulot et al., 2018; Ker et al., 2019; Colin et al., 2020a; Marsset et al., 2022). The BSR appears as an enhanced high-amplitude reversed polarity reflection, cross-cutting the stratigraphy and can be considered as a good indicator of the presence of free gas below the base of the GHSZ. Thermodynamically stable at water depths greater than ~660 m, the position of the upper limit of the GHSZ influences the current limit of the gas flare area **(Fig. 2, black dashed line and blue lines)** (Haeckel et al., 2015; Riboulot et al., 2017). However, it is important to stress that this limit has evolved over time. Riboulot et al. (2018) demonstrate that, in response to the Holocene reconnection of the Black Sea with the Mediterranean at 9k (Soulet et al., 2011b), the recent warming of bottom water temperatures (4°C to 8.9 °C) and salt diffusion in sediments provoked an important dissociation process on the shallow GH deposits. This is supported by static modelling results from Ker et al., (2019) which highlight a reduction of the GH occurrence zone associated with a seaward migration of the GHSZ upper limit since the E-LGP (Riboulot et al. 2017; Hillman et al., 2018a; Colin et al., 2020a). Secondly and more recently, Fabre et al. (2024) presented 2D dynamic modelling of the GHSZ since the last 34 ka, taking into account multi-parameters provided from in-situ measurements relative to current conditions (sea-bottom temperature, salinity, geothermal gradient), indirect assessments for past conditions (Soulet et al., 2011b), and local salt diffusion and thermal diffusivity in sediments (Riedel et al. 2020). These modelling results also indicate a potential present-day disequilibrium of the GH system in response to pressure induced by sea-level changes, bottom water temperature, heat diffusion, salinity and its downward diffusion: They show that the GHSZ remains stable between -33.5 and -20 ka (the upper limit extended from ~[495 to 525 m water-depth) (**Fig. 2, purple lines**). After -20 ka, there was a sudden back-and-forth movement of the GHSZ upper limit along the slope in response to a sea-level rise of ≤+100 m at -16 ka, before it returned to its initial position (i.e. the E-LGP position recorded between -33.5 and -20 ka)) at -15 ka due to an episode of sea-level fall (**Fig. 2, orange lines**). This was followed by a landward extension of the GHSZ reaching its maximum extent at -9 ka, in response to the last sea-level rise (**Fig. 2, yellow lines**). After -9 ka, the extension of the GHSZ drastically decreased due to bottom water warming and re-salinisation of the Black Sea. The predicted present-day GHSZ reaches its termination close to the seafloor at 660 m water (**Fig. 2, blue lines**).

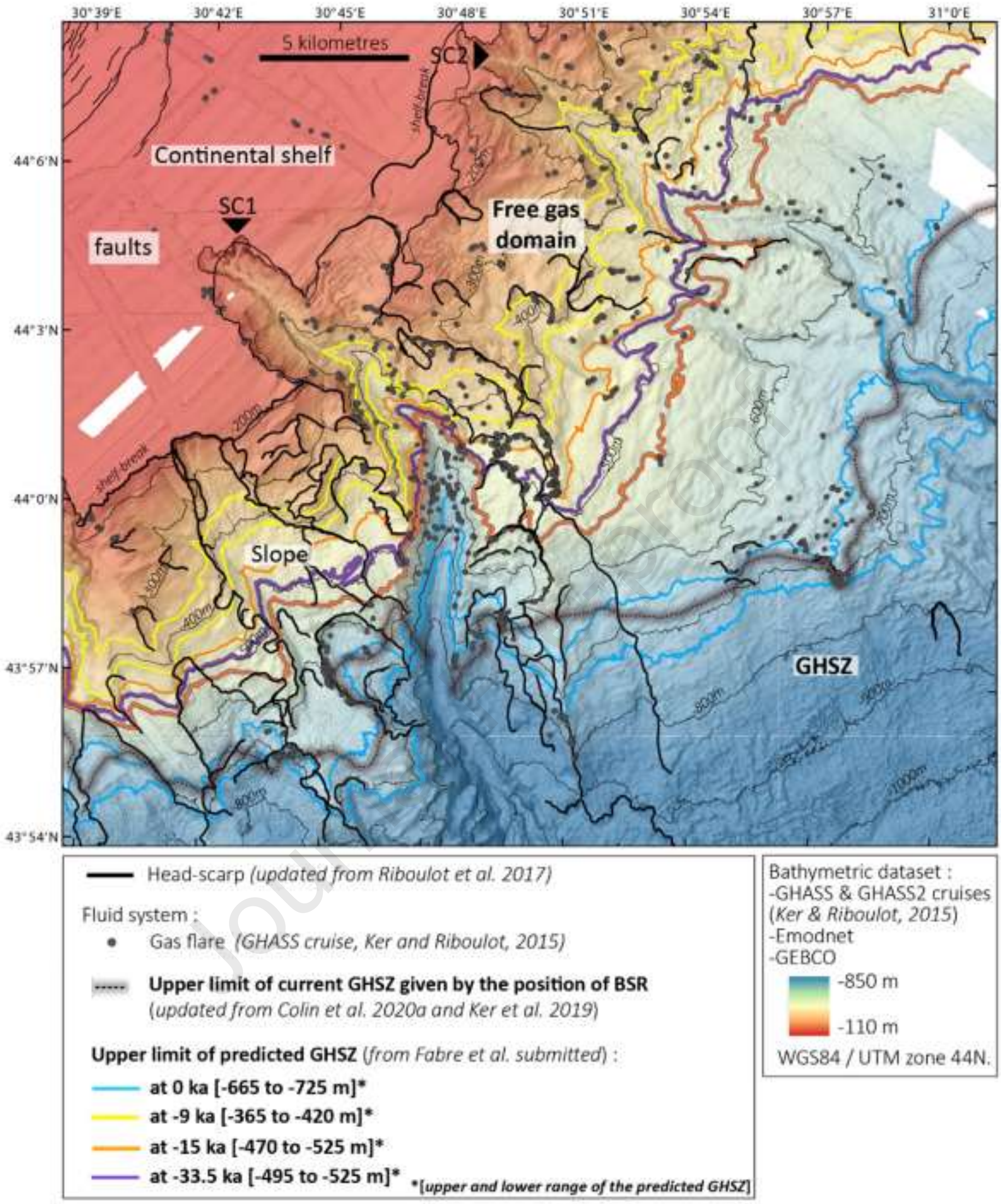

Figure 2: Geomorphologic map of the western Romanian margin, obtained from the interpretation of bathymetric data and 2D seismic data. Grey dots represent the gas flares imaged in the water column during GHASS cruise (Ker and Riboulot, 2015). We identified canyon incisions by SC1 and SC2, and bathymetric slope head-scarps (black lines, updated from Riboulot et al., 2017). The upper limit of the current Gas-Hydrates Stability Zone (GHSZ) (shaded black dashed line) has been extracted from seismic data (HR and VHR) acquired during GHASS cruise (Ker and Riboulot, 2015) from the position of the shallow Bottom Simulating Reflector (BSR) (updated from

Colin et al, 2020 and Ker et al, 2019). The upper limits of the E-LGP (purple, orange, and yellow lines) and current predicted GHSZ (blue lines) have been calculated by numerical modelling (Fabre et al., 2024). The position of predicted or observed upper limits of the GHSZ allow to distinguish the distribution of the present GHSZ, and the E-LGP GH Destabilisation zone (GHDZ) from the free gas domain.

2.5. Slope instability on the western Black Sea margin

Through a seismic-stratigraphy approach, Hillman et al. (2018b) show that the sedimentary system of the Danube Fan in the western Romanian margin is not only controlled by channel-levee sedimentation but also by significant slope-failure events incising the margin and removing some of the slope deposits. In the deep-sea fan, Winguth et al. (2000) and Popescu et al. (2001) identified multiple slumps, slides and debris flows, possibly due to high turbidity current discharging or levee breaching. In the upper slope and shelf break off the Romanian margin, many of the scarp morphologies also result from instabilities and erosion along the Viteaz Canyon headwalls. Popescu et al. (2004) suggest they formed during the last sea-level low stand, and discuss the link with gas seepage in the upper slope, and the potential role of shallow gas in sediments as a preconditioning factor for slope failure. However, none of the above-described landslides has been absolutely dated. Finally, Marsset et al. (2022), propose a detailed mapping of Mass Transport Deposits (MTDs) in the study area based on GHASS and BLASON seismic data. They evidenced a set of regional massive MTDs associated with an unconformity interpreted to be the Base Neoeuxinian Sequence Boundary formed during the last major sea-level fall. The correlation with core GAS-CS01 (Martinez-Lamas et al., 2020) indicates that this unconformity is significantly older than 34 ka (Marsset et al., 2022). Marsset et al., (2022) also mapped younger MTDs suggesting that sediment instability may also have occurred during a recent sea-level highstand. They did not correlate these later MTDs with core GAS-CS01. They propose that sediment pulses, seismicity, and gas-hydrate dynamics play determinant roles in sediment instability through time.

In this work, we complete and describe the landslide mapping carried out by Marsset et al, (2022) over the recent period from 34 thousand years ago to the present day, adding the GHASS sub-bottom profiler data and the new GHASS-2 sub-bottom profiler data acquired in 2021. This densification of data and improved resolution for recent sediments makes it possible to distinguish additional landslide phases and to optimistically correlate the main seismic reflectors with the GAS-CS01 core.

3. MATERIALS

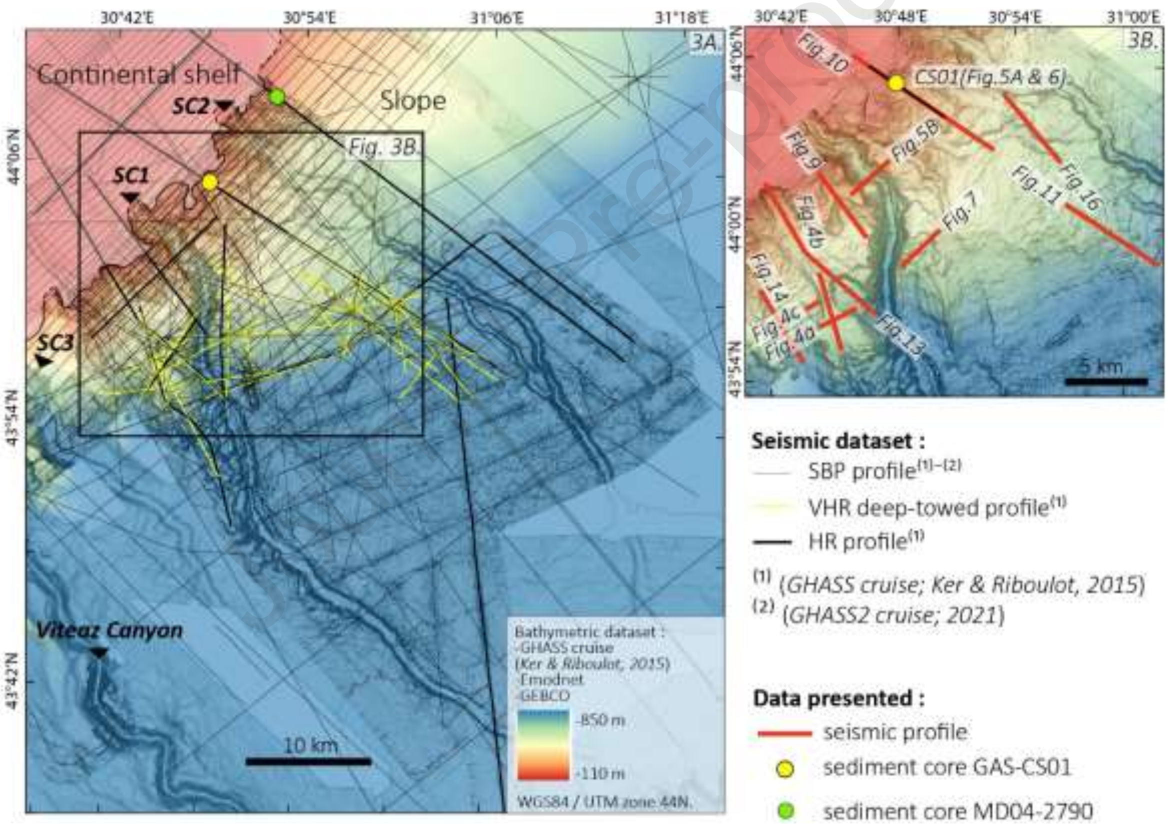

Figure 3: 3A.: Dataset used for this study, including multi-resolution seismic data, bathymetry, and sediment core data. The black bold lines represents the high resolution seismic lines (GHASS cruise, Ker and Riboulot (2015)), yellow lines correspond to the deep-towed seismic lines (GHASS cruise, Ker and Riboulot (2015)) and light black lines the sub-bottom profiler data (GHASS (Ker and Riboulot, 2015) and GHASS-2 (2021) cruises) ; SBP: from Sub Bottom Profiler, VHR: Very-High-Resolution data from SYSIF device, HR: High-Resolution data from multichannel device. 3B.: Location of seismic profiles and core GAS-CS01 (44°05.10'N, 30°47.50'E) presented in this work appear respectively with red lines and one yellow dot.

2.1. Geophysical dataset

3.1.1. Bathymetry and water-column acoustic data

This study is based on a newly compiled bathymetric map **(Fig. 1A)** including a 15-m very-high-resolution Digital Terrain Model (DTM) of the study area **(Fig. 1A, and 1C and Fig. 2)** acquired with the SMF7111 (100 kHz) and SMF7150 (12 kHz/24 kHz) multi-beam sounders from the GHASS (R/V Pourquoi pas?, Ker and Riboulot, 2015), and recent GHASS2 cruises (R/V Pourquoi pas?, 2021) and a 250-m-resolution DTM provided from *the European Marine Observation Data Network* (EMODnet) *Seabed Habitats initiative* (//www.emodnet-seabedhabitats.eu/) **(Fig. 2).**

The multi-beam echosounder SMF7111 (100 kHz) and SMF7150 (12 kHz/24 kHz) profiles acquired on the GHASS cruise (R/V Pourquoi pas?, Ker and Riboulot, 2015) and already presented in Riboulot et al. (2017), also identified the position of gas flares in the water column between the shelf and slope domain, generating regional mapping of active fluid-escape distribution on the Romanian margin presented in Figure 2. In both cases, this novel data were processed using IFREMER's Globe Software.

3.1.2. Multi-resolution seismic reflection data

All multi-channel seismic (MCS) reflection data used in this study **(Fig. 3)** were acquired during the GHASS cruise, combining multi-resolution source data (high-resolution (HR) multichannel seismic, very-high-resolution (VHR) deep-towed seismic, and sub-bottom profiler, **Table 1**). In addition, for the study, we included the sub-bottom profiler dataset acquired during the GHASS2 cruise. All profiles are newly presented in this study. The resulting dataset covers a large part of the Romanian margin from the shelf to the middle slope domain **(Fig. 3)**. Processing of High-Resolution (HR) surface and Very-High-Resolution (VHR) deep-towed seismic data was carried out with the software SolidQC® (IFREMER), SeisSpace

ProMAX®and MATLAB®, and QCSubop® (IFREMER) for sub-bottom profile quality control. Seismic profiles were interpreted on a workstation with KingdomSuite software®, and interpretations integrated into a Geographic Information System (QGIS platform®), together with bathymetric and water-column acoustic data.

3.1.2.1. High-resolution seismic data

Multi-channel seismic (MCS) reflection data **(Fig. 3)** were obtained with a small airgun source (central frequency: 110 Hz) and a 96-channel streamer with 6.25-m spacing between traces. The depth of the source and the streamer were set at 1.5 and 2 m, respectively. The penetration of this acoustic signal reaches ~ 500 m below the seafloor (mbsf) with a resolution in the order of 3.5 m vertically and between 15-25 m horizontally **(Table 1)**. It images the deep geometry of the slope and the BSR zone. MCS profiles were mostly obtained by applying a conventional post-stack processing sequence. For specific profiles, a pre-stack depth migration was performed after migration velocity analysis (Ker et al., 2019).

3.1.2.2. Very-High-Resolution (VHR) deep-towed seismic data

To image the sedimentary architecture in detail and investigate the GHSZ, we used the VHR deep-towed seismic reflection data **(Fig. 3)** from the IFREMER SYSIF system (Ker et al., 2014; Marsset et al., 2014). Towing both the source and streamer at 50-100 m above the seafloor provides an improved lateral resolution, lower sensitivity of 3D effects and a better signal-to-noise ratio. This system works with a very-high-resolution source (220 Hz -1050 Hz) and a 52-channel streamer with 2 m spacing and obtains seismic data with a vertical resolution of less than 1 m, with penetration up to 200 mbsf **(Table 1)**. Recent developments have allowed fine-scale velocity analysis to determine P-wave velocity distribution, down to 50-100 mbsf thanks to streamer length (Colin et al., 2020b; Marsset et al., 2018). For greater depth, the velocity field required for depth migration is defined with neighbouring HR data analysis.

3.1.2.3. Very-high-resolution sub-bottom profiles

A total of 344 sub-bottom profiles cross the shelf edge and were acquired along HR seismic profiles **(Fig. 3)**. The CHIRP source operates at a frequency-modulated signal ranging between 1800 Hz and 5000 Hz to obtain an infra-metric vertical resolution with optimal penetration at 80 mbsf **(Table 1)** for precise correlation with long piston-core data collected in the study area.

Acoustic specifications / **Seismic source**	**Frequency range (Hz)**	**Vertical resolution (m)**	**Horizontal resolution (m)**	**Penetration (mbsf)**	**Interest for this work**
MCS (HR)	45-170	3.5	15 m	500	Deep architecture of slope system
Deep-towed seismics (VHR)	220-1050	<1	2 m	150-200	Characterisation of landslides geometry
Sub bottom profiler	1800-5000	0.5	15 (for 800 m water depth)	80	Characterisation of landslides geometry Correlation with core data and dating

Table 1: Specifications of seismic reflection data used for this study.

2.2. Sediment core

Constraining geophysical observations with core data allows to deduce the lithological succession and information on the ages of landslide units observed in the study area.

Sedimentology data comes from the Calypso long-piston core GAS-CS01 (44°05.10N, 30°47.50E) collected during the GHASS cruise (R/V Pourquoi pas?, Ker and Riboulot, 2015) at 240 m water depth from the shelf margin, ~40 km east of the Danube Canyon head, i.e. between northern canyons SC1 and SC2 **(Fig. 3)**.

The 32.1-m-long core GAS-CS01 records the regional lithological succession of the western Black Sea, and has been described in detail by Martinez Lamas et al. (2020). This lithological succession, observed from the western Black Sea upper slope (Bahr et al., 2005; Major et al., 2002; Soulet et al., 2011a) to the Danube deep-sea fan (Constantinescu et al., 2015), consists, at the surface, of marine Unit I (Marine Cocoolith Ooze (MCO), <2720 ± 160 cal a BP) and

Unit II (sapropel, deposited from 8,080 ± 250 cal a BP) and below, lacustrine Unit III described by Ross and Degens (1974). Core GAS-CS01 therefore contains a very-high-resolution record of the marine and glacial lacustrine Units I, II and III (until ca. 33.5 ka) (Martinez-Lamas et al., 2020).

Through the correlation of their respective XRF-Ca records (Soulet et al., 2011a; Martinez-Lamas et al., 2020), the GAS-CS01 calendar age-depth model, between core-depth intervals 253 cmbsf to 1595 cmbsf, is based on that of core MD04-2790 (N 44°12.8′, E 30°59.6′), collected at 352 m water depth, ~19.6 km east of GAS-CS01 during the ASSEMBLAGE cruise (2004) (refer to Supplementary materials *Table 2* in Martinez Lamas et al., 2020). This calendar age-depth model was reconstructed with an alignment approach of the TEX86-derived Lake Surface Temperature with the Hulu Cave $\delta^{18}O$ speleothem record (Wang et al., 2001). Below the depth 1595 cmbsf, chronology is based on radiocarbon age ^{14}C yr BP (Dreissena sp. and bulk organic matter) bounding back to ~34 ka at the base of the core (3214 cmbsf). Lastly, no dating is available above 253 cmbsf, at the top of core GAS-CS01 (refer to Supplementary materials *Table 2* in Martinez Lamas et al., 2020). However, identification of a 20-30-cm-thick Sapropel layer, well-documented and identified as the ‘lacustrine’ Unit II in the western Black Sea margin (Ross and Degens, 1974; Soulet et al., 2011a; Constantinescu et al., 2015) can be considered as a temporal reference interval for our study, deposited from 8,080 ± 250 cal a BP (Soulet et al., 2011a).

4. METHODS

2.1. Seismic stratigraphy and correlation with core GAS-CS01

Analysis of the available seismic database **(Fig. 3)** provided the very-high-resolution sedimentary architecture of the upper slope of the Romanian margin, and thus highlights the relative chronology of the different landslides which highly imprint the seafloor **(Fig. 2)**.

Based on seismic stratigraphic principles, we firstly identified major discontinuities and depositional units derived from reflection terminations (erosional truncations, onlaps, downlaps), seismic facies and geometric analysis (Mitchum et al., 1977). This consequently led to identifying successive erosional and remoulded landslide seismic units interstratified between continuous and conformable sediment successions **(Fig. 4)**.

Four distinct major reflectors **R**(X), corresponding to conformable correlative surfaces, were selected and followed along the entire dataset. They were identified in MCS and deep-towed profiles by continuous, high-amplitude reflectors, and, by strong contrasts in the sub-bottom profiles. We were consequently able to distinguish different seismic units labelled U1 to U5 (from oldest to youngest) (**Fig. 4C**), with concordant, continuous and parallel reflectors. **R**(X) reflectors have been propagated towards core GAS-CS01 (**Fig. 5**). In some areas, they are truncated by younger MTDs (**Fig. 4B**). To explore landslide occurrence and study their distribution on the western upper slope, the depths of the **R**(X) reflections and respective basal surfaces of each landslide unit were checked at all tie-points and tracked interactively over the whole dataset.

When dating MTDs, we considered that failure events occurred during a time lapse bounded between the youngest MTD truncated seismic reflector and the first deposits overlying MTDs**.** Dating MTDs with calibrated ages equates to correlating seismic observations with dating information extracted from the 32.1 m long Calypso piston core GAS-CS01 **(Fig. 5)**, positioned on the northern side of the canyon SC1 **(Fig. 3)**, in a sector where strata were preserved from erosive/landslide surface processes **(Fig. 5).**

Propagating and comparing seismic observations on both sides of the canyon SC1 through different crossing points (from profile to profile), favours a robust correlation strategy **(Fig. 5B)**.

Next, for each landslide, we correlated the youngest eroded reflector and top MTD surfaces with the GASC01 core for which the lithological facies and age-model are published (Martinez-Lamas et al., 2020) **(Fig. 6)**.

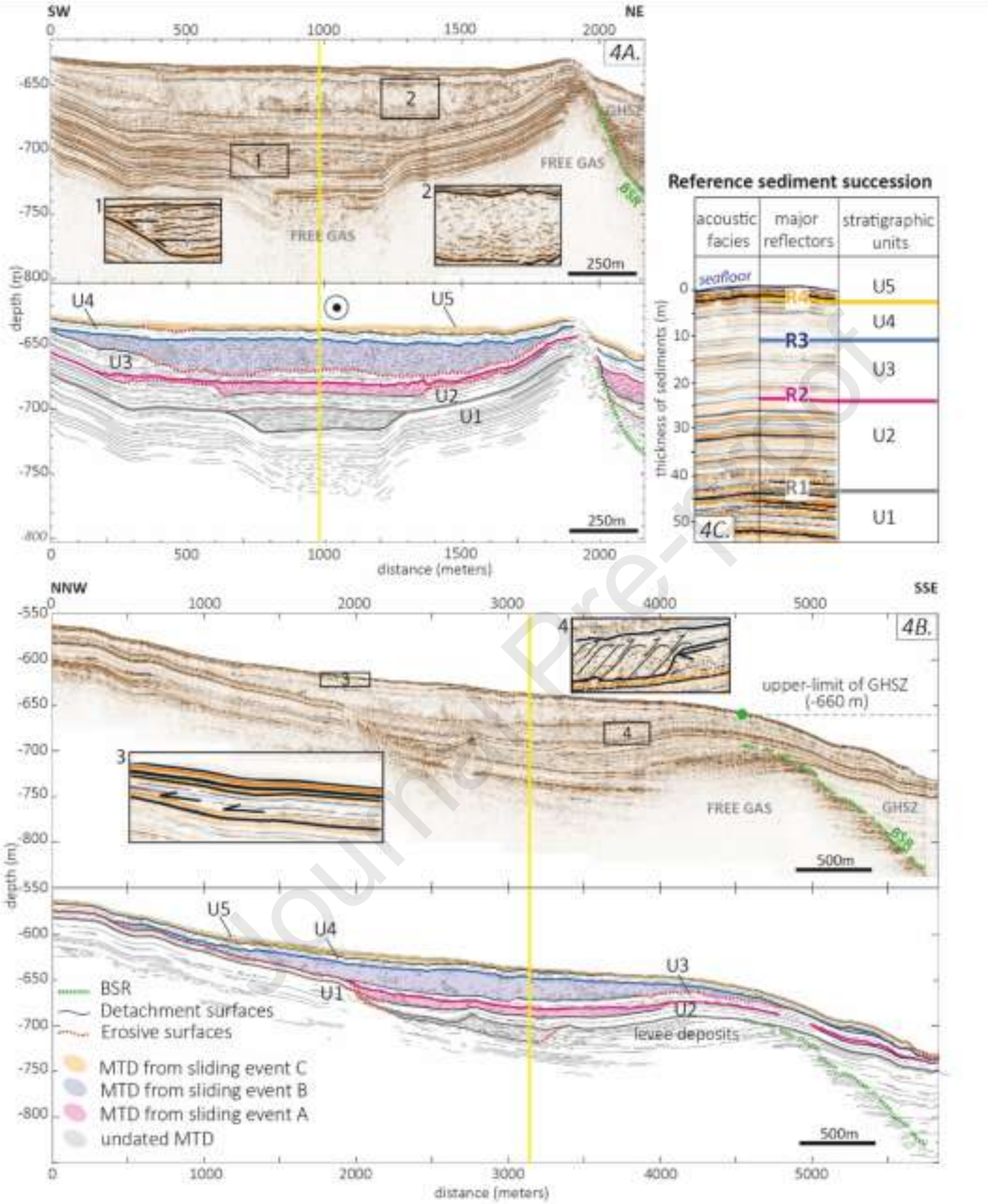

Figure 4: Presentation and interpretation of seismic very-high-resolution deep-towed profiles to describe different landslide events on the upper slope of the study area (4A.: PR01PL06 for transversal point of view and 4B.: PL01PR02 for longitudinal point of view). Profile presented on Figure 4A. crosses over the profile in Figure 4B. (yellow line). The MTDs, identified by seismic chaotic to transparent units with low amplitude and discontinuous reflectors have been coloured. The inserts 1 to 4 show the detail of the acoustic characteristics of the different MTDs and their internal organisation. They erode and contrast with conformed units highlighted by line drawing.

Details of unit U(X) typology and positions of reflector R(X) are presented on the stratigraphic reference profile (PL03PR02) on the Figure 4C. The dashed green line marks the position of the Bottom Simulating Reflector (BSR), which cross-cuts the stratigraphy at the top of enhanced reflectors with high amplitude, and represents the interface between free gas and the hydrate reservoir. Seismic data shows that MTDs generally extend above the upper limit of the actual BSR -660m), and their glide planes are very superficial in comparison with the present-day BSR. Lines location reported in Figure 3B.

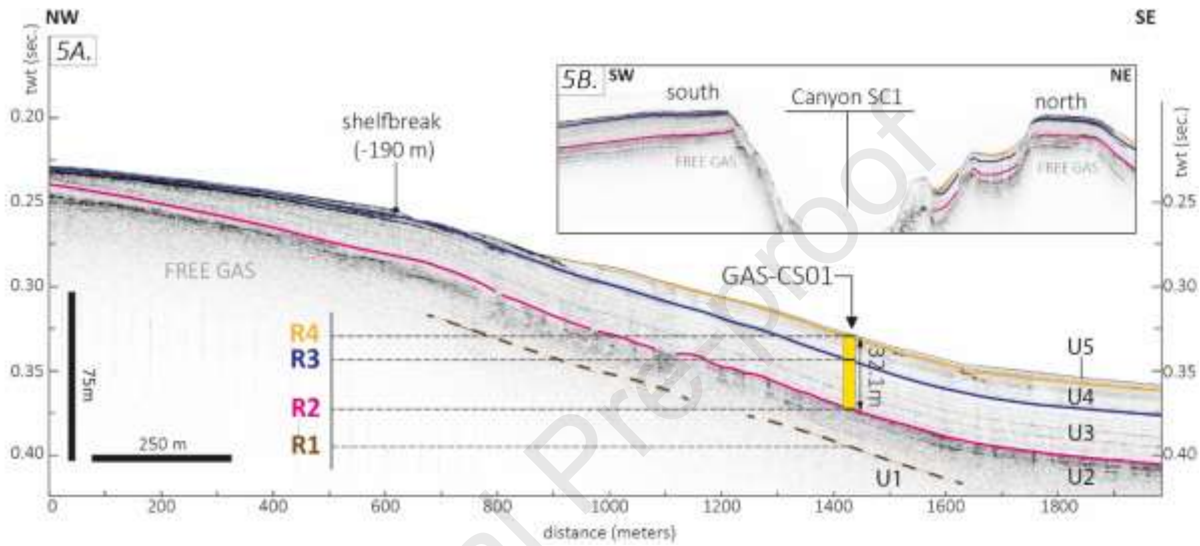

Figure 5: 5A.: Propagation of the regional reflectors R1, R2, R3 and R4 (Fig. 4), from failure zone to the VHR sub-bottom profile GAS-SDS031b (Fig. 3), and correlation with the 32.1 m long core GAS-CS01 (GHASS cruise, Ker and Riboulot (2015)). The core GAS-CS01 is positioned on the northern side of the SC1 (Fig. 3). As shown in 5B., (profile GAS-SDS-0015) the correlation from profile to profile required the propagation of seismic reflectors on both sides of the SC1 though multiple crossing points in between different seismic sections. SBP n° GAS-SDS-0031b (5A) and GAS-SDS-0015 (5B) locations are reported in Figure 3B.

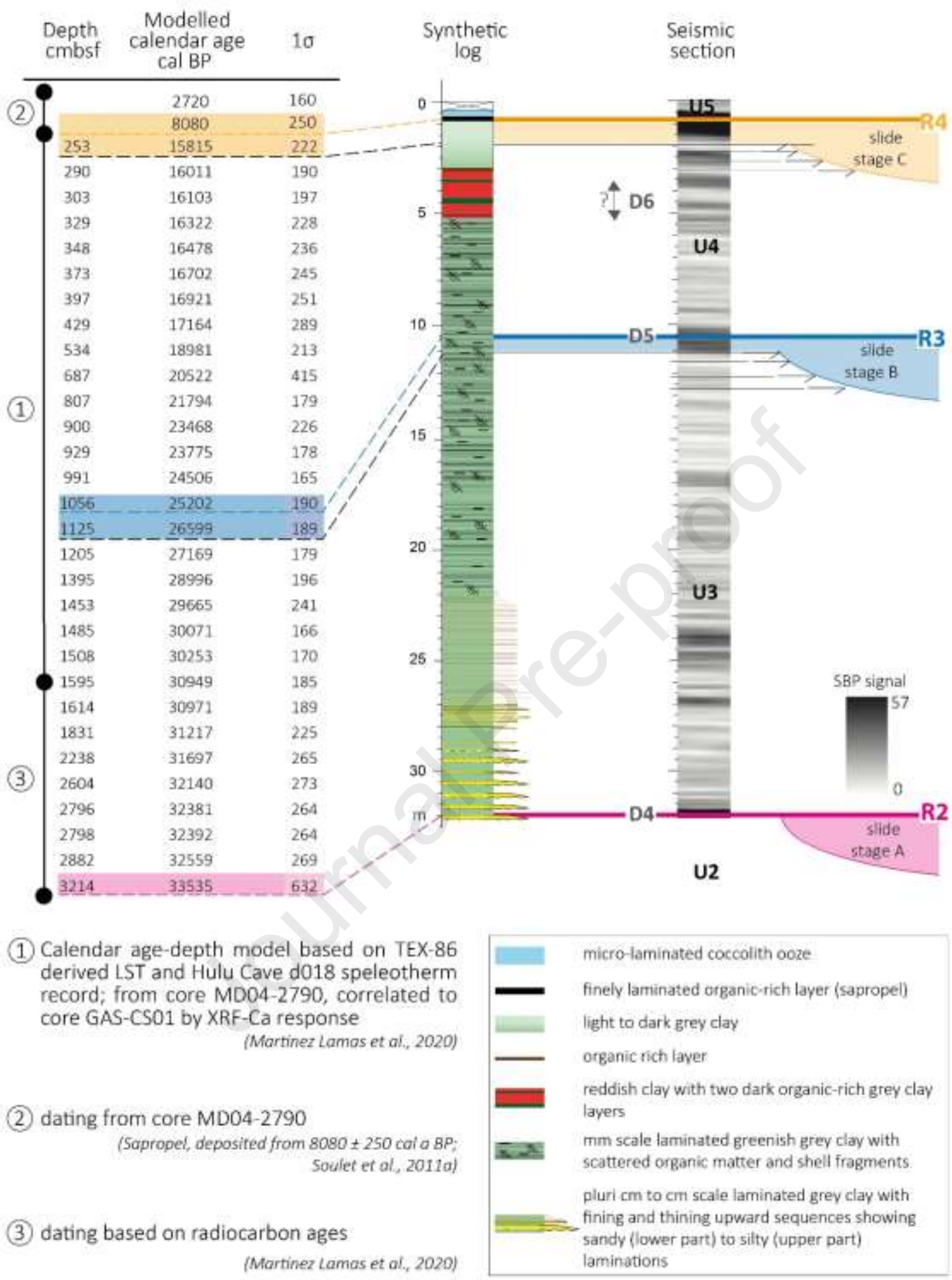

Figure 6: Regional lithological succession, given by core GAS-CS01 (Fig. 3). Core chronologies from core GAS-CS01 are presented and compared with the very-high-resolution sub-bottom profile (SBP) GAS-SDS031b presented in Figure 5. ① Between 253 cmbsf until to the depth 1595 cmbsf, the GAS-CS01 calendar age-depth model provided from Martinez-Lamas et al., 2020, with standard deviation 1σ. It is based on a correlation with the calendar age-depth model of core MD04-2790 (N 44°12.8', E 30°59.6') established by Soulet et al., 2011a,

(collected ~19.6 km east of GAS-CS01 during ASSEMBLAGE cruise (Lericolais, 2004)), reconstructed with alignment approach of TEX86-derived Lake Surface Temperature with the Hulu Cave $\delta^{18}O$ speleothem record (Wang et al., 2001). ② No published dating have been established above 253 cmbsf; however, the 20-30 cm thick Sapropel layer, identified as the 'lacustrine' Unit II in western Black Sea margin is deposited from 8,080 ± 250 to 2.720 ± 160 cal a BP, derived from core MD04-2790 by Soulet et al., 2011a. ③ Below the depth 1595 cmbsf, the chronology is based on radiocarbon age ^{14}C yr BP (Dreissena sp. and bulk organic matter) bounding back to ~ 33,500 cal a BP at the base of the core (3214 cmbsf) (Martinez-Lamas et al., 2020). Chronological constraints from core GAS-CS01 are compared with the well logs representing described lithological facies. On the right, a simplified sketch which explains the method used to date landslides considering dated regional reflectors R(X) as sealing the chaotic units and representing the first deposits not-affected by the deformation. Thus, assigning them a calendar age provides data on the maximum age of failure events A, B and C. The locations of SBP profile and core GAS-CS01 are presented in Figure 3B. in the study area; The entire SBP profile is presented in figure 5.

2.2. Thickness and surface models of mass transport complexes

By digitalisating the top and basal MTD surfaces, we created isochron maps of the identified Mass Transport Complexes (MTCs, made of multiple MTDs), which were computed by means of the "flex-gridding" algorithm on the KingdomSuite-software toolbox. In view of the objective of this article, and the available chronostratigraphic constraints (Martinez et al., 2020, Soulet et al., 2011b) we computed thickness and surface models only for landslides that occurred since 33.5 ka (E-LGP to present). For grid interpolation, the closest to the thickness information, we chose the convex hull method to define the calculation bounds. Smoothing of data was required to correct the outliers of side effects. Isochron maps allow to calculate surface and thickness statistics and represent the lateral extent of each landslide regarding the distribution of scar failures highlighted by the bathymetric data. The two-way-travel-time-to-depth conversion (Twtt in seconds to metres) considered a water velocity and surficial sediments of 1480 m/s provided from sonic cone in-situ measurements made during the GHASS cruise (Ker and Riboulot, 2015). It is important to note that for failure zones initiated directly near the canyon, part of the reworked masses were transported towards the canyon and were not systematically preserved. This consequently prevents an accurate evaluation of total removed sediment volumes.

5. RESULTS

Submarine landslides in the study area engender morphological evidence on the seafloor **(Fig. 2).** Nevertheless, the presence of landslide head scarps on bathymetry does not imply recent instability. Age can be understood only through seismic stratigraphic analysis and correlation of core data.

Some chaotic units are identified on seismic data by similar general geometry and an acoustic signature as presented in Figure 4. They display lenticular geometries.

Most landslide units are characterised by the same general geometry and acoustic signature. They are represented by lenticular geometries of varied size (Fig. 4), and interstratified between continuous and conformal reflection packages (Fig. 4). In MCS and deep-towed data, these units are characterised by low-amplitude chaotic facies, discontinuous and hummocky reflectors (Fig. 4 inserts 1, 2, 3) and by transparent facies in sub-bottom profiles. In some cases, it is possible to identify internal reverse faults **(see insert 4 in Fig. 4)**, which suggest gravitational contraction, generally at the distal part of the MTDs. Their basal surface is generally erosional grading, laterally to conformal.

We distinguished failure events (events A, B, C) characterised by contemporary individual MTDs **(Fig. 4).**

2.1. Dating of MTDs

Numerous buried MTDs that were not reached by GAS-CS01 (Fig. 5) could not be absolutely dated. In turn, the failure event A, sealed by **R2** was dated at a minimum age of 33,500 cal a BP **(Figs. 4 and 6)**. The failure event B, sealed by **R3**, was dated between 26,600 and 25200 cal a BP **(Figs. 4 and 6)**. Finally, **R4** seals the failure event C. Since **R4** corresponds to the top of the Sapropel unit observed on GASCS01 and dated at 8,080 cal a BP by Soulet et al. (2011a), we associated the failure event C to the period included between 15,800 cal a BP and 8,080 cal a BP (**R4**) **(Figs. 4 and 6)**.

2.2. MTDs older than 34 ka

A series of MTDs are positioned below **R2**, thus older than -33,500 cal a BP **(Figs. 6 and 7).** They are all sealed by a ~ 80-m-thick bedded sedimentary strata **(Fig. 7)** characterised by low to high-amplitude reflectors interrupted by thin landslides (example in Figure 7, in yellow, an MTD older than 34 ka, and in pink, a younger MTD). Their thicknesses vary between ~40 and 110 m and their basal surfaces are erosive and truncate deeper units. Younger sediments and MTCs overlie these MTDs without completely filling the head scarps, therefore they still have surface expression **(Fig. 8, associated head scarps underlined in black on bathymetry).** MTDs older than 34 ka and associated head scarps are located along the head walls of canyons SC1, SC3 and SC2 between 190 m to >1500 m water depth **(Fig. 8)**. They result in around twenty head scarps, 1.5 to 3 km wide, easily perceptible on seafloor morphology, and account for 80% of the present-day scar failures identified in bathymetry. For example, a major head scarp along the south SC1 canyon edge located below 560 m water depth, presents a well-defined circular shape, ~2.5 km wide and more than 3 km long, creating a negative offset/incision 80 m high (**Fig. 8**, black box, studied by Hillman et al., 2018b). These events are clearly identified on some MCS and deep-towed seismic profiles, labelled as ‘regional MTD’ but are not detailed in this article (see Marsset et al., 2022 for more information on these events, older than 34 ka).

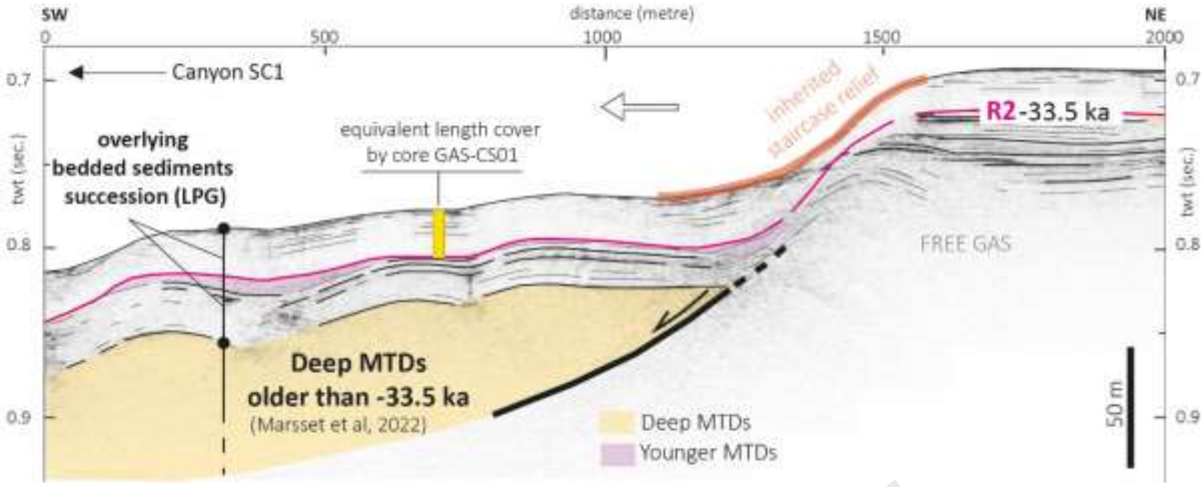

Figure 7: Geometry of deep MTDs older than 34 ka, identified in the SC1 canyon edge. These chaotic units are generally characterised by lenticular units. Their basal surfaces are erosive and truncate deeper units. In sub-bottom profiler data, they appear as transparent acoustic bodies. Those deep MTDs are sealed by younger sediments . Additional small remobilized units that occurred after -34 ka, presented in this study, are interbedded (MTDs coloured in pink) within this draping cover. Note that post-bedded sediments and recent MTCs overlay the deep MTDs without completely filling the head-scarps. The length of core-GAS-CS01 has been added in the SBP section to show the depth investigated for dating in this study (Fig. 6). SBP n° GAS-SDS-0010 location is reported in Figure 3B.

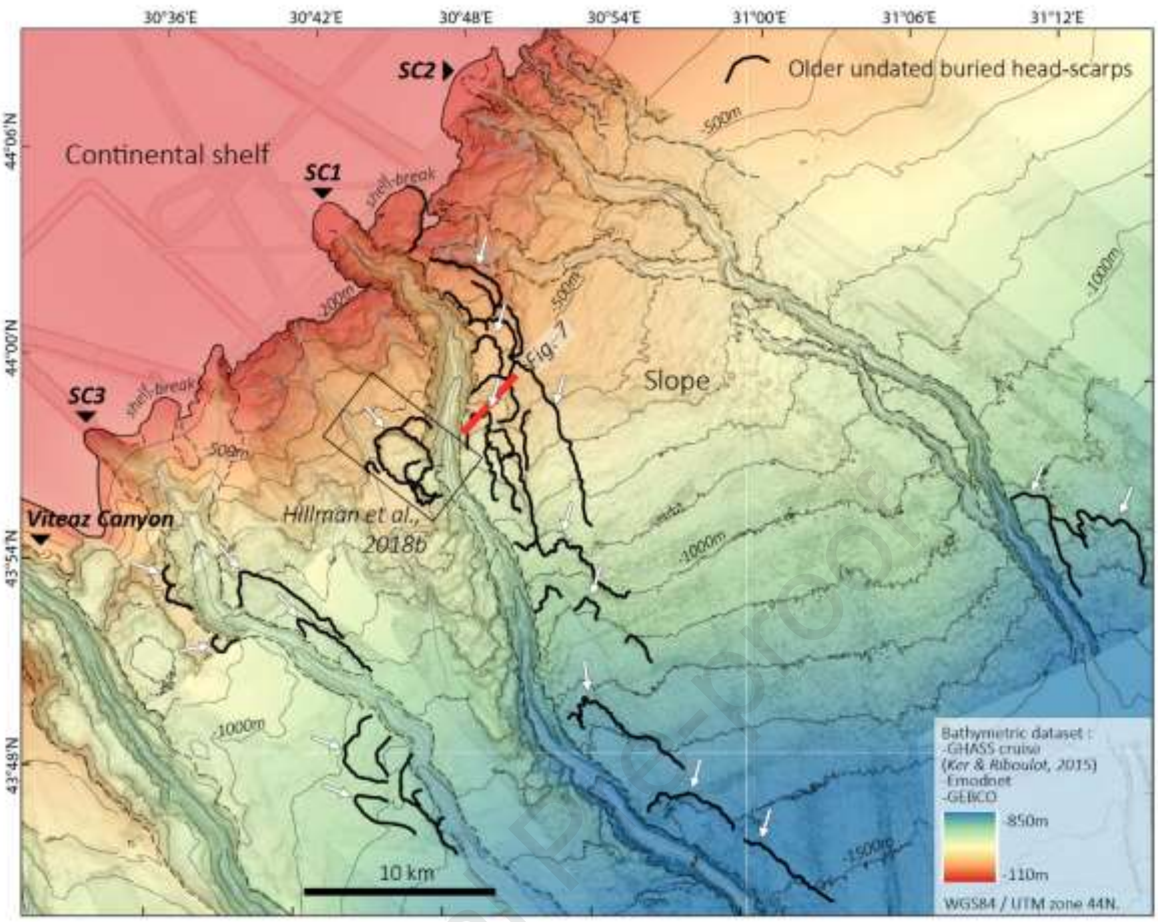

Figure 8: Distribution of head-scarps related to failure events older than 34 ka (black lines) (Fig. 7A.). Note that they generally extend in the north and south SC1 canyon edge, between the shelf break domain at -190 m and -1500 m. No head-scarps related to this older stage have been identified along the canyon SC2 edge. According to the orientation of the scar, the destabilised sediments (white arrows) discharged directly in the canyon.

2.3. 'Surficial' landslides initiated after -34 ka

3.1.1. Failure stage A

3.1.2.1. Main characteristics of seismic and sub-bottom profiler data

The failure event A, sealed by **R2 (Figs. 4 and 6)**, is composed of several synchronous MTDs deposed at 33,500 cal a BP during the E-LGP. As shown in **Figure 4**, this Mass Transport Complex (MTC)-A gathers MTDs characterised on MCS and deep-towed data by a transparent to chaotic seismic facies, with low to medium amplitude and discontinuous hummocky reflectors. On sub-bottom profiles, they usually appear with transparent acoustic facies **(Fig. 9)**. The basal surfaces of MTDs belonging to MTCs-A display irregular surfaces and unconformities **(Figs. 4B, 9, and 10A-10B)** in seismic data. In head-scarp zones, these landslides incise **U2 (Figs. 4, 9, and 10A)**, locally **U1**, and older deep sediments in the northern part **(Fig. 10A).** In many cases, the basal surfaces of MTC-A are not clearly identified in the failure area because of signal perturbation due to high free-gas content approaching the shelf break **(Fig. 10)**. However, we highlight that this major event in the north part of the study area has truncated sediments up to ~ 80 m and remoulded large amounts of sediments seaward, down to 1500 m water depth **(Figs. 10 and 11B).** Going downslope, MTC-A MTDs evolve in lenticular units that are characterised by transparent acoustic facies, without internal coherent organisation of sediments. These lenticular units show erosional or conformal bases **(Fig. 10C).**

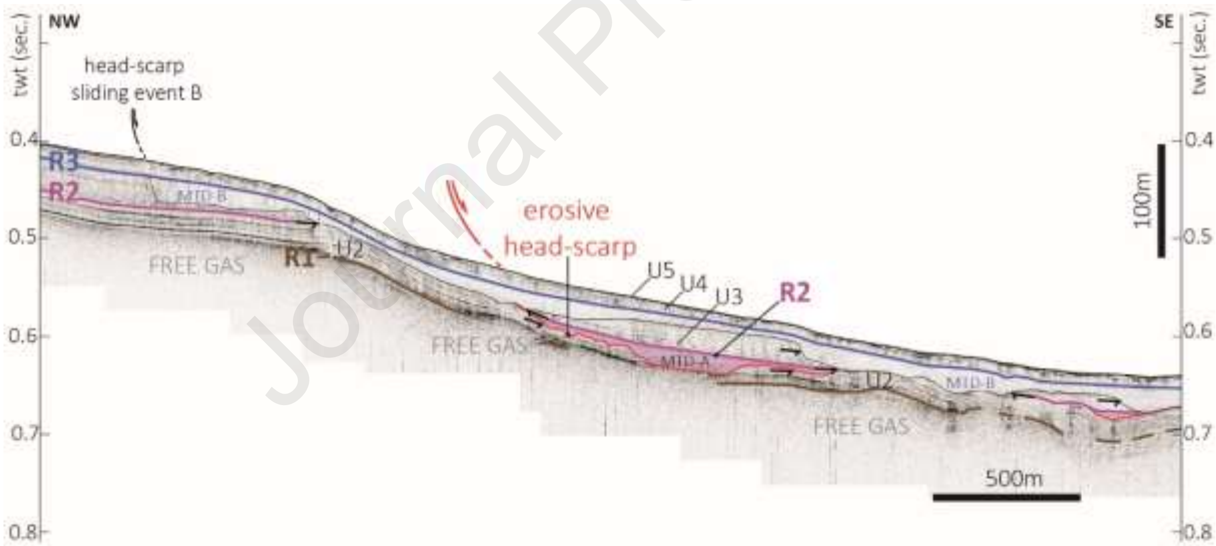

Figure 9: Typical upslope to downslope evolution related to the failure stage A at 33,500 cal a BP, on a sub-bottom-profiler (SBP) profile n° GAS-SDS-038. SBP location is reported in Figure 3B. Upslope, this MTC is characterised by an erosional basal surface connecting to an erosive failure zone (roughly located as "erosive head-scarp") that initiated in the south SC1 canyon edge (zone (1) in Fig. 12A.). Erosional truncations are represented by black arrows. Downslope, the associated MTD (coloured in pink) basal surface evolves towards a less erosional system, correlating with a stratigraphic detachment layer characterised by a conform and

continuous reflector. Seismic units and regional reflectors are labelled U(X) and R(X) respectively, according to the typology defined in figure 4C.

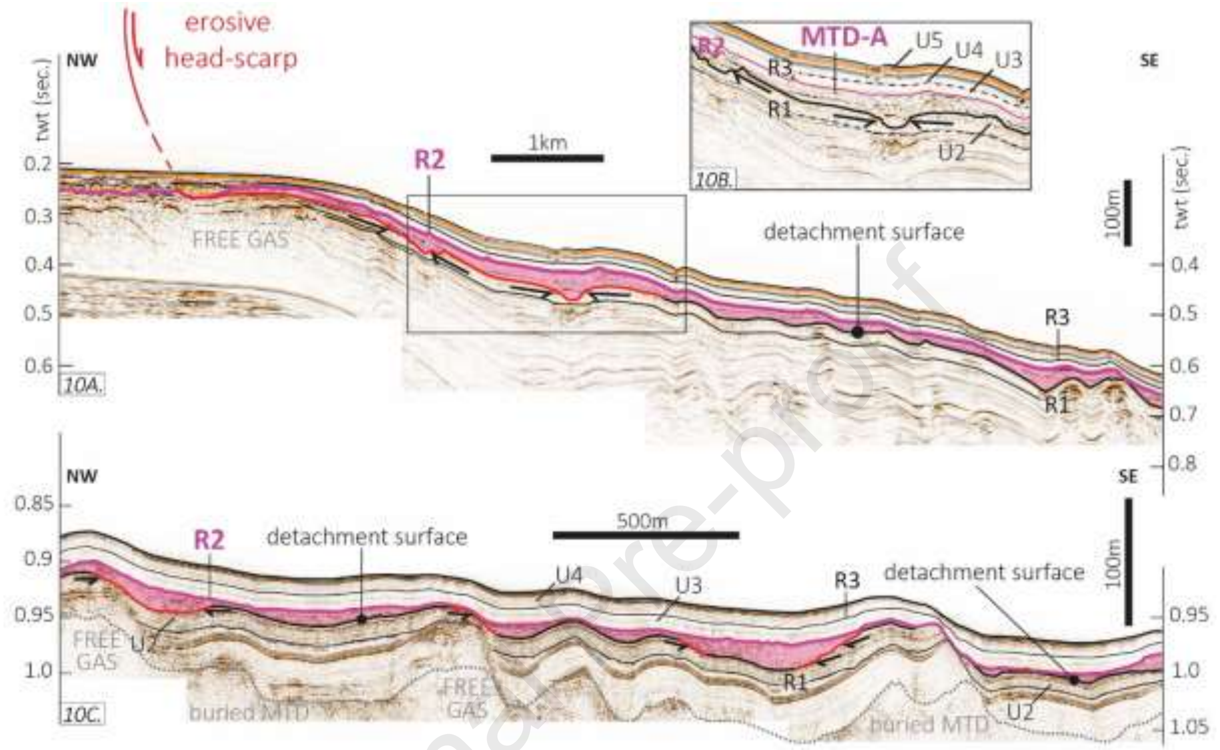

Figure 10: Typical upslope to downslope evolution related to the failure stage A at 33,500 cal a BP, 10A. and 10B.: on a MCS line n° mig031, and 10C.: on a VHR deep-towed seismic line n° PL03PR07. MCS and VHR deep-towed seismic lines locations are reported in Figure 3B. 10A: Upslope, this MTC is characterised by an erosive failure zone (erosion domains underlined in red, erosional truncations represented by black arrows) that resulted in a massive MTC (coloured in pink) that extended between -190 m and -1500 m (zone (3) in Fig. 12A.). This MTD is characterised by chaotic facies in comparison with non-affected bedded sediment succession, as showed in 10B. 10C.: Going downslope, the basal MTC surface evolves toward a stratigraphic detachment layer, characterised by a conform and continuous reflector (detachment layer underlined in black). Seismic units and regional reflectors are labelled U(X) and R(X) respectively, according to the typology defined in figure 4C.

3.1.2.2. Spatial distribution and thicknesses

Failure stage A consists of several MTDs, which differ in their location and size **(location and extension in Fig. 11A).** They mostly initiate along the shelf-break edge and along SC1 and

Viteaz canyons (**Fig. 11A**). The MTCs-A represents a cumulative surface up to ~910 km² with thicknesses ~7 m on average, reaching ~105 m in the northern part **(Fig. 11B).**

We observed a lateral evolution of MTC-A from west to east **(Fig. 11B)**: in **zone (1)** near the head of the Viteaz Canyon. Large MTDs initiated along the flanks of the canyon axial talweg; in **zone (2)**, along the western side of canyon SC1. Small MTDs initiated along the canyon edge forming new elongated head scarps associated with transported lobate deposits. Their mean thickness is ~5 m with a maximum of ~26 m **(Fig. 11B).** In **zone (3)**, along the eastern side of canyon SC1, MTDs initiated along the canyon edge, reactivating older head-scarp incisions **(Fig. 8)**. In these areas, MTC-A represents 60 km² of the MTC-A total surface and are characterised by low mean thicknesses of ~6 m with a maximum of ~28 m **(Fig. 11B).** The sediment movements of MTC-A in **zones (2)** and **(3)** show two major flow directions: a north-west/south-east flow on the western-headwall of canyon SC1 and a north-east/south-west flow on the eastern headwall of canyon SC1.

Finally, in **zone (4)**, along canyon SC2, a major MTD related to the failure stage A **(Fig. 11A)** has been mapped on both sides of the canyon. It seems to initiate along the shelf edge. This MTD represents more than 80% of the total MTC-A surface with a regional extent of 760 km²**.** It is 45 km long, and 23 km wide, and is bounded at the south by canyon SC1 levees and progressively disappears northward **(Fig. 11A).** MTC-A can be subdivided **(Fig. 11B)** into different sediment distribution areas: upslope, starting from the shelf break at -190 m, MTC-A displays large thickness patches, (**Fig. 11B**, in yellow). Further downslope, accumulation zones consist of thinner lenticular units, infilling pre-existing depression morphologies inherited from an underlying regional MTD (described by Marsset et al., 2022) **(Fig. 10C).** Seaward, accumulation decreases between -700 m and -1200 m water depth, thinning drastically between -1200 m and -1500 m, and totally disappearing under 1500 m water depth **(Fig. 11B).**

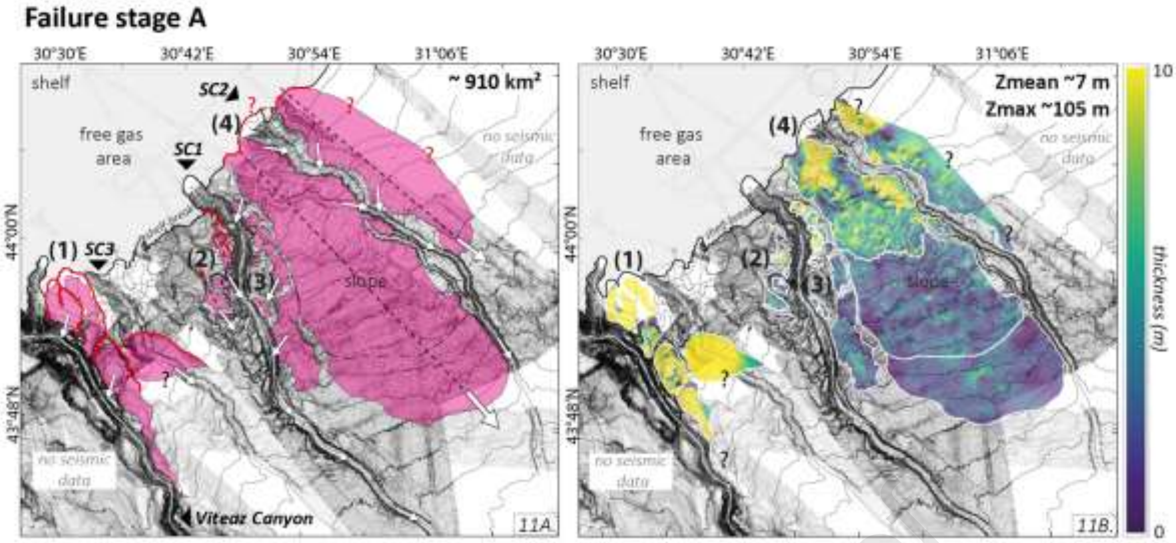

Figure 11: 11A. Spatial distribution of MTDs related to the failure event A (coloured in pink). The major head-scarps are digitalized in red (bold lines). Dashed black lines and white arrows represent respectively major and local directions of mass wasting. 11B. Isochron map of MTC-A obtained by subtracting the basal surface and the top of MTC-A. The thickness colour-scale is in metres. Twtt has been converted in depth considering a water velocity of 1480 m/s provided from in-situ measurements. White lines in Figure 11B. represent the limits of individual MTDs within MTC-A defined by Figure 11A. Information about interpolation calculation are detailed in the section 4.2. Thickness and surface models of MTCs.

3.1.2. Failure stage B

3.1.2.1. Main characteristics on seismic and sub-bottom profiler data

Failure event B consists of several synchronous MTDs that occurred during the E-LGP, between 26,600 and 25,200 cal a BP, sealed by R3 **(Fig. 6)**. MTC-B are characterised by discontinuous and low-amplitude reflectors with chaotic configuration in MCS and deep-towed data **(Figs. 4 and 12)**, and by transparent responses in the sub-bottom profiler **(Fig. 13).** The basal surfaces of these MTDs **(Fig. 4)** incise **U3,** and **U2** as attested by the presence of erosional truncations in the head-scarp zone **(Figs. 12A and 13).** The top of these MTDs can be irregular as shown in **Figure 12B**.

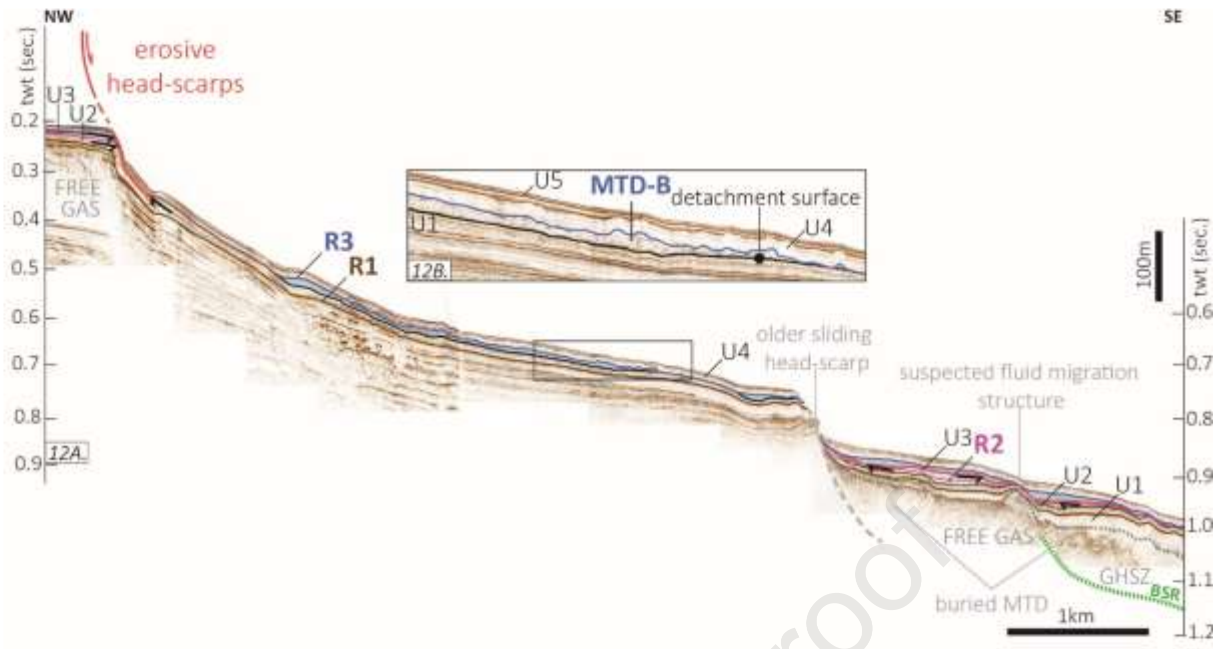

Figure 12: Typical upslope to downslope evolution, related to the failure stage B, that occurred between 26,600 and 25,200 cal a BP, on a MCS line n°mig033b and a VHR deep-towed seismic line n° PL01PR03. Location of MCS and VHR deep-towed seismic lines locations are reported in Figure 3B. 12A.: Upslope, near the shelf-edge and downslope, near inherited head-scarps, the base of MTC-B is erosive (underlined in red, erosional truncations represented by black arrows). Laterally, the basal surface of MTC-B evolves to a stratigraphic detachment layer, characterised by a conform and continuous reflector (basal surface underlined in black). This MTC is characterised by chaotic facies in comparison with non-affected bedded sediment succession, as showed in the insert 12B. Seismic units and regional reflectors are labelled U(X) and R(X) respectively, according to the typology defined in Figure 4C.

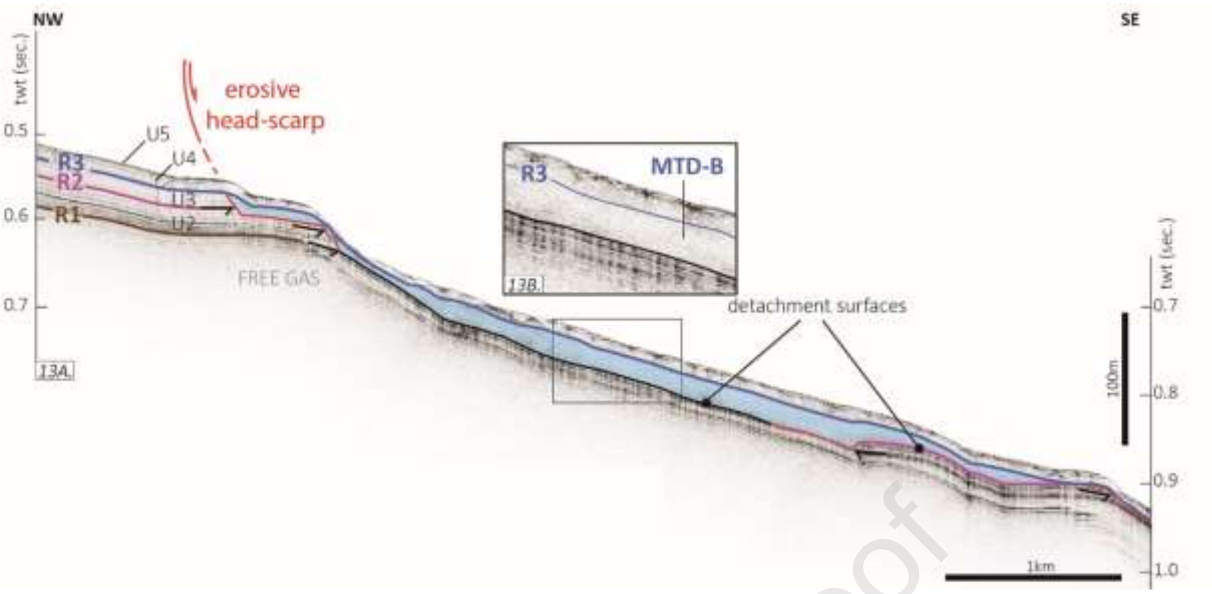

Figure 13: Typical upslope to downslope evolution, related to the failure stage B, that occurred between 26,600 and 25,200 cal a BP, on a VHR sub-bottom profile (SBP) n° GH2-SDS-028B. SBP location is reported in Figure 3B . Upslope, near the shelf edge and downslope, near inherited highs, the base of MTC-B is erosive (underlined in red, erosional truncations represented by black arrows). Laterally, the basal surface of MTC-B evolves to a stratigraphic detachment layer, characterised by a conform and continuous reflector (basal surface underlined in black).This MTC is characterised by transparent facies in comparison with non-affected bedded sediment succession, as showed in the insert 13B. Seismic units and regional reflectors are labelled U(X) and R(X) respectively, according to the typology defined in Figure 4C.

3.1.2.2. Spatial distribution and thicknesses

MTC-B affect the upper slope domain between 200 m and 700 m water depth and represent a cumulative surface of ~145 km² of reworked sediments **(location and extension in Fig. 14A)**. Most MTC-B failures initiate along the shelf edge or the very upper slope. Some of them initiate along SC1 and Viteaz canyons. A few of them (labelled **(5)** in **Figure 14A**) initiate in the middle slope domain. In most cases, they form a series of individual landslides, the upper part of which is narrow and evolves into a lobed landslide mass. The associated MTDs are ~6 m thick on average, reaching 48 m locally **(Fig. 14B)**, Close to 90% of the MTC-B total surface is situated along the Viteaz, SC1, SC3 canyon edges **(zones (1), (2) and (3) in Figure 14A)**. There, associated slope failures consist either in individual neo-formed head scarps, that highly incised the seafloor between 200 m and 450 m water depth **(zones (2) in Fig. 14A)**, or large inherited head scarps located on the north Viteaz-Canyon flank **(zone (1) in Fig. 14A) (Figs. 12 and 13)**. In the north of SC1 canyon edge, the failure event B did not generate massive MTDs contrary to the failure event A.

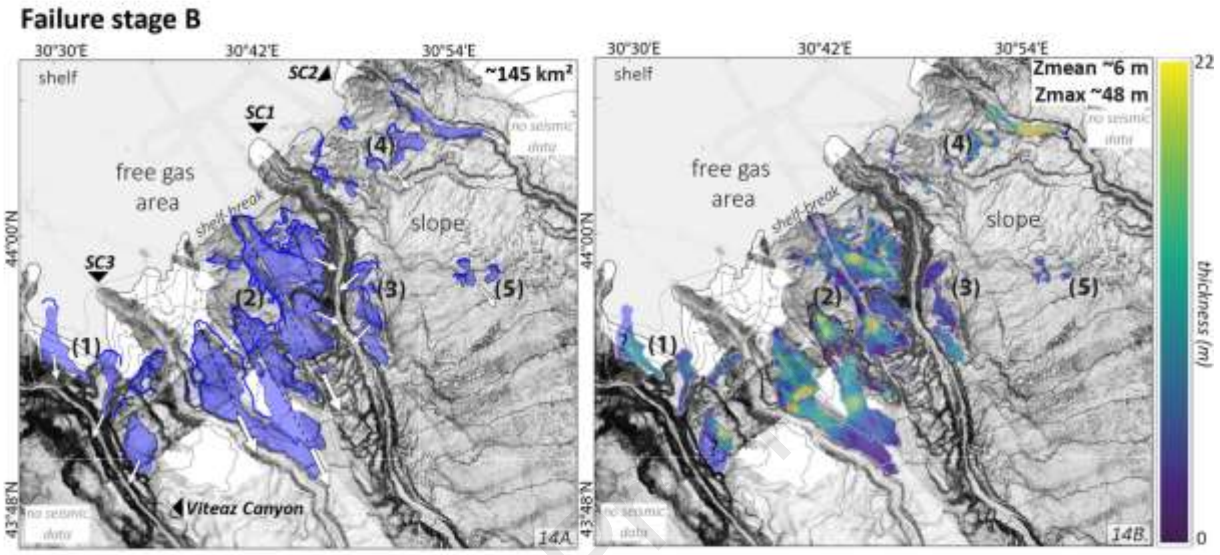

Figure 14: 14A. Spatial distribution of MTDs related to the failure event C (coloured in blue). The major head-scarps are digitalized in blue (bold lines). Dashed black lines and white arrows represent respectively major and local directions of mass wasting. 14B. : Isochron map of MTC-B obtained by subtracting the basal surface and the top of MTC-B. The thickness colour-scale is in metres. Twtt has been converted in depth considering a water velocity of 1480 m/s provided from in-situ measurements. White lines in Figure 14B. represent the limits of lateral extension of MTC-B defined by the Figure 14A. Information about interpolation calculation are detailed in the section 4.2. Thickness and surface models of MTCs.

3.1.3. Failure stage C

3.1.2.1. Main characteristics on seismic and sub-bottom profiler data

The failure event C is the last to occur in the study area, between 15,800 cal a BP and 8,080 cal a BP **(Fig. 6).** It resulted in several synchronous very thin MTDs that truncated surficial sediment layers **(Figs. 4 and 15).** MTC-C, related to failure event C, are overlain by the thin bedded unit **U5** (0-0.4 mbsf) (**Fig. 15),** which constituted the last and more recent deposits in the study area (Soulet et al., 2011a; Martinez Lamas et al., 2020), equivalent to marine Unit I described by Ross and Degens, (1974). MTC-C are sealed by reflector **R4**, **(Figs. 4 and 15)** a strong and enhanced reflector in the sub-bottom profiler data (**Fig. 15**), which corresponds to Sapropel deposits (Unit II from Ross and Degens, 1974) dated to 8,080 ± 250 cal a BP (Soulet et al., 2011a) **(Fig. 6)**. The basal surface of MTC-C MTDs is erosional, as attested by the presence of erosive truncation incising **U4 (Fig. 15)**.

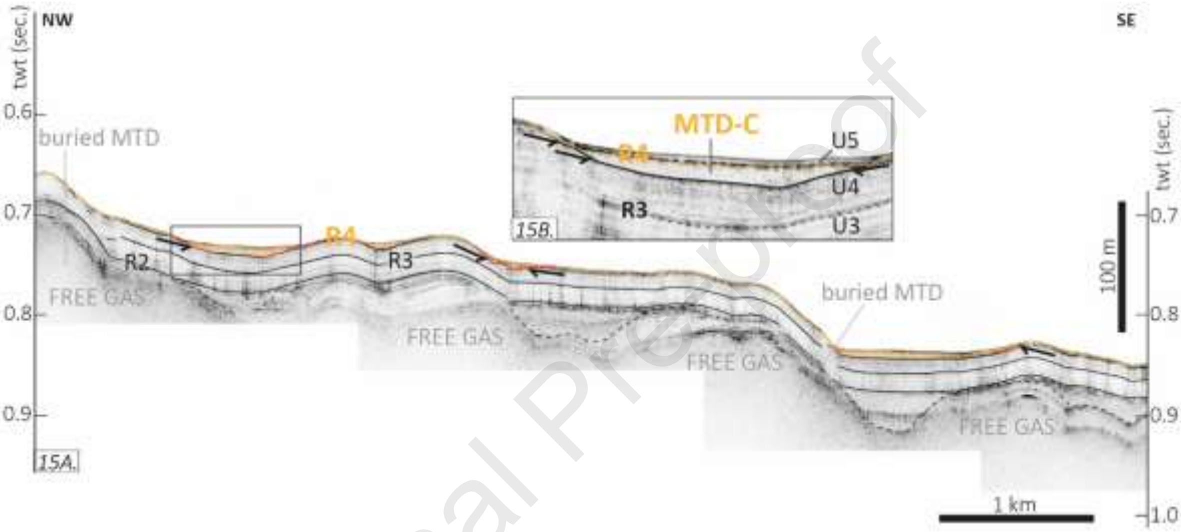

Figure 15: Typical upslope to downslope evolution, related to the failure stage C that occurred between 15,800 and 8,080 cal a BP, on a VHR sub-bottom profile (SBP) n° GH2-SDS-047A. SBP location is reported in Figure 3B. 15A.: The base of MTC-C is, depending on areas either erosive (underlined in red, erosional truncations represented by black arrows), either it evolves to a stratigraphic detachment layer, characterised by a conform and continuous reflector (basal surface underlined in black). This MTC is characterised by transparent facies in comparison with non-affected bedded sediment succession, as shown in the insert 15B. Notice that this MTC-C is the thinnest that we mapped (3 m in average). It is only visible on SBP data. Seismic units and regional reflectors are labelled U(X) and R(X) respectively, according to the typology defined in Figure 4C.

3.1.2.2. Spatial distribution and thicknesses

The major part of scar failures associated with MTC-C occurred between the shelf break and ~700 m water depth for the deepest head scarp (**Fig. 16A).** They are associated to elongated MTDs, some of them following canyon paths (along SC2, SC3 and canyons imprinted in bathymetry between SC1 and SC2) (**Fig. 16A**). In many cases, MTC-C slope failures reactivated older ones.

No major MTD related to this stage has been identified directly on the flank of the Danube-Viteaz Canyon contrary to MTC-A and MTC-B failure events **(Figs. 11 and 14)**. MTC-C represents a total surface of ~148 km² (**location and extension in Fig. 16A.**), with a thickness of ~ 3 m on average, reaching ~30 m in the south SC1 canyon edge **(Fig. 16B).**

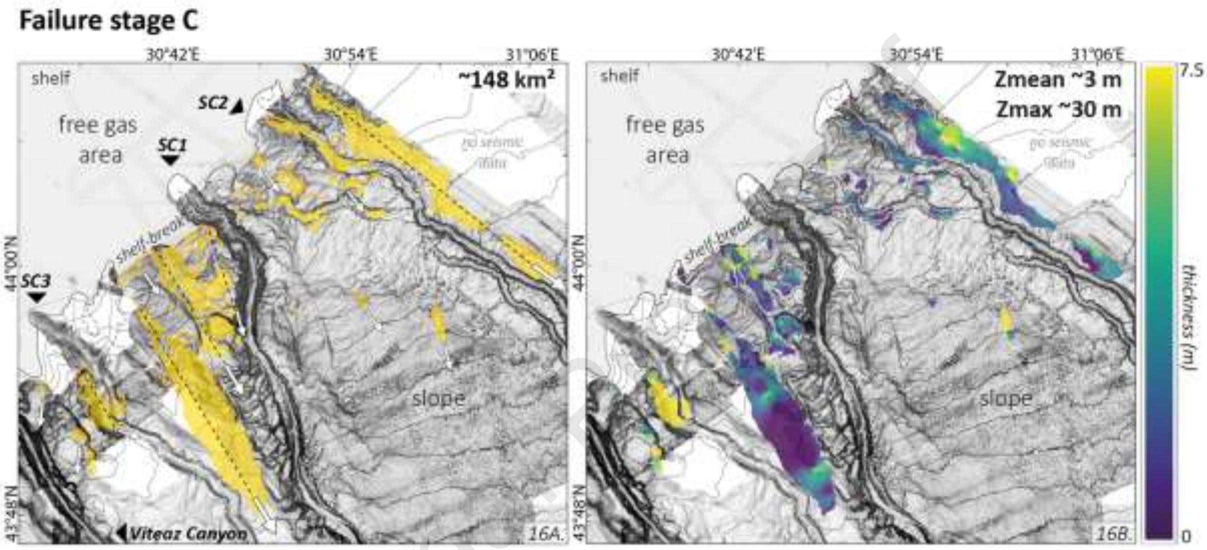

Figure 16: 16A. Spatial distribution of MTDs related to the failure event C (coloured in yellow). The major head-scarps are digitalized in yellow (bold lines). Dashed black lines and white arrows represent respectively major and local directions of mass wasting. 16B : Isochron map of MTC-C obtained by subtracting the basal surface and the top of MTC-C units. The thickness colour-scale is in metres. Twtt has been converted to depth considering a water velocity of 1480 m/s provided from in-situ measurements. White lines in Figure 16B. represent the limits of lateral extension of MTC-C defined by the Figure 16A. Information about interpolation calculation are detailed in the section 4.2. Thickness and surface models of MTCs.

2.4. Characterising MTD basal surfaces

MTD basal surfaces evolve laterally for all MTDs. Except for the failure zones, where erosional truncations of underlying sediments are clearly discernible (***Erosive head-scarps*** **in Figs. 9, 10A, 12, 13 and 15**), MTD basal surfaces always evolve to conformable surfaces along specific stratigraphic planes. In seismic data, they correspond to continuous high-amplitude reflections

(**Figs. 9, 10B, 12, 13, and 15).** Six major MTD basal surfaces have been identified, and their extension has been tracked in the study area; they are labelled **D1**, **D2**, **D3**, **D4**, **D5** to **D6** as represented in **Figure 17** along a schematic profile view. The deepest, **D1** served as a detachment layer during the failure event B **(Fig. 17). D2** and **D3** acted as detachment layers for failure events MTC-A and MTC-B. **D4** (i.e. **R2**) and **D5** (i.e. **R3**) were activated respectively by the failure events of MTC-B and MTC-C. Finally, **D6** was used as a detachment layer for the surficial failure event C **(Fig. 17).** Regarding coring information **(Fig. 6)**, **D1**, **D2** and **D3** were not reached by GAS-CS01 core. D4 corresponds to **R2**, located at 0.045 s Twtt on the seismic section **(Fig. 5)**; it seems to correspond to the top of a pluri-centimetre scale sandy layer, at the interface with a grey-clay sequence, that is to say a high permeability layer below a lower permeability layer. **D5** corresponds to **R3** collected at 0.014 s Twtt (i.e. 10.5 mbsf) which seems to be associated with millimetre-scale laminated greenish-grey clay facies with scattered organic matter and shell fragments. Finally, **D6** is located in the Red Layer interval **(Fig. 6)** between 0.33 s Twtt and 0.328 s Twtt (i.e. between 3.5 to 5.2 mbsf) which corresponds to a series of four individualised intervals of reddish-brown clays and are thought to represent the sedimentary imprints of the meltwater inputs that occurred during Heinrich Stadial 1 (HS1) (Soulet et al., 2013).

Regarding the relation between these slope failures and the fluid system in the western Black Sea margin, we remarked that nearly all landslides initiated above the present-day GHSZ **(Figs. 11, 14, 16)**. We also observed that the basal shear surfaces are particularly surficial and activated along stratigraphic intervals located above the top of the free-gas domain, well identified in seismic data by an extended acoustic blanking zone **(*free gas* in Figs. 9, 10A, 12, 13 and 15).**

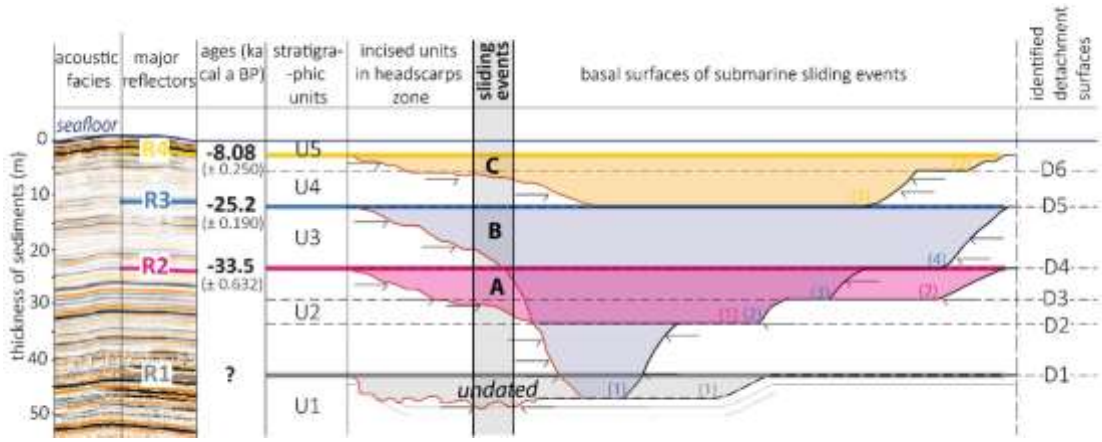

Figure 17: Diagram representing the chronology of the different failure events in the study area and details of units and basal stratigraphic detachment surfaces identified on seismic data. Note that it's a schematic view of the entire study area. Reflectors R(X) correspond to the first deposits non-affected by successive landslides and give the maximum age of the failure event (i.e. Figs. 4 and 6). Basal surfaces are represented by erosive surfaces in the failure areas which erode the seismic units U(X). Identified reflectors D(X) act as detachment surfaces along stratigraphic planes, and may have activated several times for different failure events ; In this case, orders (small numbers) are assigned for each detachment plan with corresponding slide colour. For example, D2 can be used as detachment plane firstly during the failure event A (1) and later somewhere else by the failure event B (2). Six major stratigraphic detachment planes have been identified in the study area. Note that some of them, such as D4 and D5, correspond to equivalent R(2) and R(3). The ages correspond to the dating of R2, R3, R4 extracted from core GAS-CS01 (Fig. 6).

6. DISCUSSION

2.1. Uncertainties in the slope failure model age

The slope failure model age presented in this study considers well-constrained dating established on core GAS-CS01 by Martinez-Lamas et al., (2020). We have taken account of the uncertainties that may persist due to the vertical correlation between geophysical data (plurimetric for MCS to sub-metric resolution for deep-towed and sub-bottom profiler data) and sediment coring data (millimetre resolution) and we cannot exclude small shifts in our correlation (max. 50 cm, which is the vertical resolution of sub-bottom profiler data). However, we are confident in the correlation we propose since the enhanced acoustic response of reflectors **R2**, **R3**, and **R4**, which sealed and dated the successive MTCs (**Fig. 4**), seems to be correlated with sediment lithological changes provided by the lithofacies log which is well-identified on core GAS-CS01 **(Fig. 6)**. We considered a maximum error of 50 cm and thus ~150 yr for the age of MTC-A, <500 yr for the age of MTC-B (see age model and core length on Figure 6). The age of MTC-C is constrained by the absolute age of Sapropel.

Overall, these minimum and extended time frames provide sufficient information to consider the possible links between GH dissociation and slope-failure stages (next section). Indeed, MTC-A and MTC-B clearly occurred during the low sea-level stage associated with the E-LGP **(Fig. 18)** and MTC-C occurred during the complex phase of reconnexion between the Black Sea and Mediterranean Sea **(Fig. 18).**

2.2. Preconditioning factors

3.1.1. Role of thin permeable layers in gas storage

The distribution of gas flares observed in the water column of the study area is generally in agreement with the extent of free-gas areas, outside the GHSZ, (Popescu et al., 2007 and Riboulot et al., 2017), between the shelf domain and the upper slope down to 660 m water depth **(*Free gas domain* in Fig. 2).** Here, free-gas seepages occur along a complex fault system that extends across the shelf domain, and along discontinuities and deformation areas, especially canyons and older heads-scarp incisions (Riboulot et al., 2017, Hillman et al., 2018b) **(Fig. 2)**. On the presented seismic data **(Figs. 9, 10, 12, 13, and 15)**, the gas appears as acoustic blanking domains as already described by Hillman et al. (2018b), Riboulot et al. (2017) and Ker et al. (2019) (**Figs. 9, 10A, 12, 13, and 15),** or vertical gas-migration structures (Hillman et al., 2018b).

The formation of transient gas reservoirs in mud-confined and coarse-grained units has been described as a factor favouring submarine instabilities or sediment softening in pockmark fields, as investigated in the Norwegian margin (Plaza-Faverola et al., 2010), in the South China Sea (Sun et al., 2012), and the Nigerian margin (Riboulot et al., 2013).

Based on seismic data and sediment core information, we were able to define several possible transient gas-storage zones in the study area, characterised in seismic data by very reflective surfaces and positioned along stratigraphic planes (**Figs. 9, 10, 12, 13 and 15**). Given the position of the identified MTC detachment planes **D4** (i.e. R2) **D5** (i.e. R3), and **D6** (**Figs. 6 and 17**), the potential gas-storage zone in core succession corresponds either: to sandy layers at the base of the core (interval between 29 to 32 mbsf), along beds with shell fragments (interval between 5 to 22 mbsf), or, to organic matter-rich layers (that may form a source of biogenic gas) trapped within the reddish-brown clays (interval between 3.5 to 5.2 mbsf) (Soulet et al., 2013) (**Fig. 6**). These layers are generally localised between clay-rich less permeable layers, that possibly played the role of impermeable caprock and trapped quantities of free gas, as already proposed elsewhere by Dugan (2012), Chatterjee et al. (2014), Plaza-Faverola et al. (2010), Sun et al. (2012), and Riboulot et al. (2013).

3.1.2. Climate forcing and high sedimentation rate

Correlating the initiation time of the three failure stages with the regional sea-level curve (Soulet et al., 2011a; Constantinescu et al., 2015) **(Fig. 18A)** has allowed us to reconstitute the chronology of the failure events in relation to the evolution of Black Sea environmental conditions.

The failure events A and B, dated to [33,500 ±632 cal a BP] and [26,600 ±189 cal a BP to 25,200 ±190 cal a BP] respectively, occurred during the E-LGP (Constantinescu et al., 2015), when the Black Sea was a giant freshwater lake, and low-stand conditions dominated with a lake level ~100 m to 150 m below the present one, significantly reducing the Danube River mouth distance to the shelf edge (Deuser 1972; Soulet et al., 2010; Lericolais et al., 2011; Wegwerth et al., 2016), **(Fig. 18A)**. Identification of rhythmic layering throughout the core

GAS-CS01 (Martinez-Lamas et al., 2020) has provided insights into the river flood record in the western Black Sea over the ca. 33.5-15 ka interval. The authors define the main periods of increases in the frequency of hyperpycnal turbidite deposits (hyp.250 yr^{-1}), each of 1.5-3 ka duration (Martinez-Lamas et al, 2020), and indicate enhanced surface melting of the Alpine Ice-Sheet during Heinrich Stadial 3 (ca. 32-29 ka), Greenland Stadial 4, and HS2 (ca. 26-23.5 ka) (Martinez-Lamas, et al., 2020).

The failure events B and C seem to occur during or right after successive acceleration of river flood frequency at the Danube River mouth **("*F1, F2, F3, F4, F5*" in Fig. 18B)**. These flooding episodes suggest increasing Danube sediment discharge and could be considered as a climate forcing event to explain rapid sedimentation on the shelf edge during a stage of progradation, resulting in excess pore pressure constituting a preconditioning factor to failure.

An increase in sediment supply on the upper-slope domain is supported by a significantly high sedimentation rate, estimated at ~ 340 cm/ka at the base of Core GAS-CS01 between 33,500 and 29,000 cal a BP, with a maximum at 31,000 cal a BP, reaching 900 cm/ka **(Fig. S1 in Supplementary Material)**. The failure event B occurred 900 yrs after the end of the flooding event **(F4) (**ca. 29-27.5 ka) which recorded >50 hyp.250 yr-1 by the Danube River (Martinez-Lamas et al., 2020) and, attested by the location of the scar failures, initiated particularly close to the shelf break at -190 m water depth, from the north Viteaz Canyon flanks.

After failure event B, the sediment succession recorded in core GAS-CS01 indicates relatively low sediment rates on the upper slope at this period (between 1.40 m/ka and <1m/ka) **(Fig. S1 in Supplementary Material) (Fig. 14).** After 15.7 ka, the disconnection of the Danube River mouth and the Viteaz Canyon, in response to the sea-level rise, led the sediment depocenter to move landward on the shelf, and to a decrease in sediment supply on the upper slope (Constantinescu et al., 2015). The sediment accumulation rate recorded after 15,800 cal a BP at site GAS-CS01 (< 30 cm /ka) is very low. This could explain the relatively smaller thickness of the individual MTDs **(Fig. 16A)** in comparison with massive MTDs that occurred during failure stages A and B.

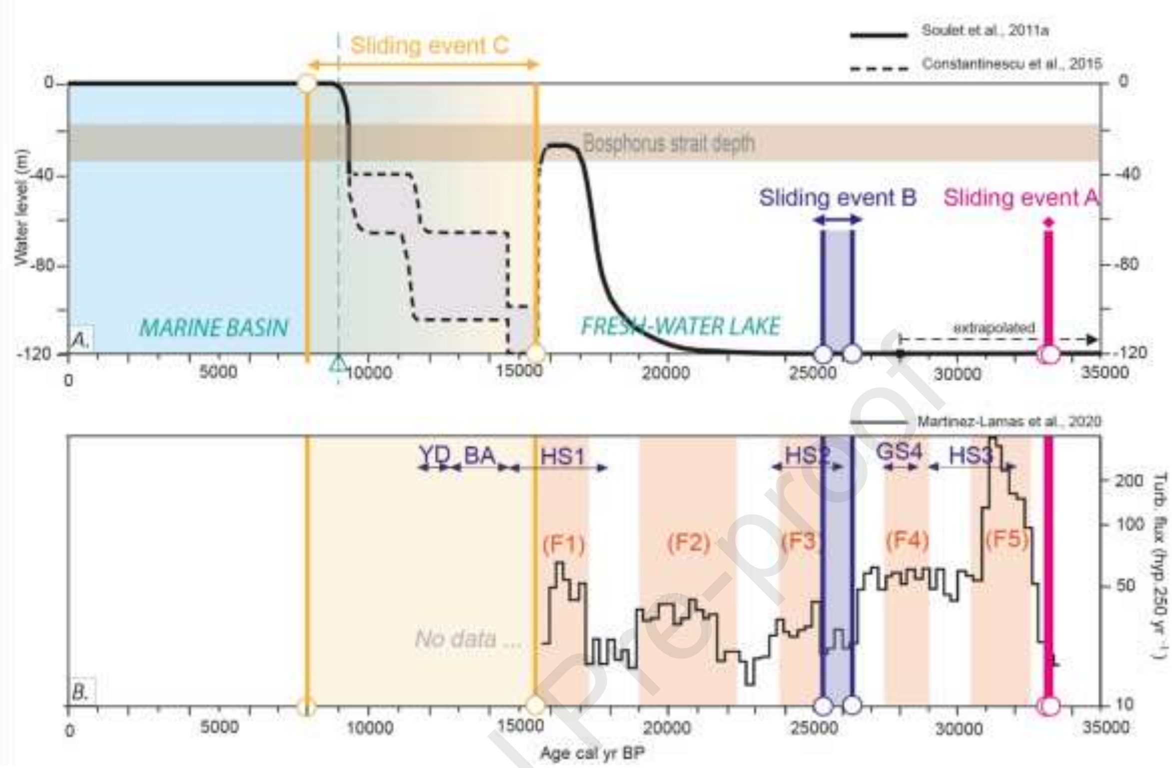

Figure 18: 18A. The timing of failure event activation in comparison with the Black Sea-level curve since the E-LGP; the sea-level curve is provided by Constantinescu et al. (2015), modified by Soulet et al. (2011a). They define the lowstand period between -28 ka and -20 ka, with a sea-level of ~120 m below the present-day level. Sea-level rise episode related to the Fennoscandian glaciers melting discharge between -17.2 ka and -15.7 ka (Soulet et al., 2013; Constantinescu et al., 2015; Toucanne et al., 2009), followed by an important evaporation stage with a possible last sea-level fall between -100 m and -120 m (Matsoukas et al., 2007, Soulet et al., 2011, Constantinescu et al., 2015). Finally, the last sea-level rise in response to the last global interglacial warming occurred in the upper Pleistocene and Holocene, induced by the reconnection of the Black Sea with the Mediterranean Sea. The failure event A and failure event B occurred during the lowstand period. The failure event C, the youngest, is synchronous with the lake-to-marine transition due to the last sea-level rise, when the Black Sea freshwater lake evolved to an open marine basin environment through flooding of the Bosphorus strait. 18B. : The flood frequency (Black indented curve), measured in previous study along the Core GAS-CS01 (Martinez-Lamas et al., 2020) is based on both the flood frequency and the Sediment Accumulation Rate (SAR) of the Danube River (Figure S1 in Supplementary Material) interpreted as periods of enhanced flux of sediment-laden meltwater on the northwest Black Sea margin. The vertical light orange bars highlight the timing for the F5 (32,500 to 30,500 cal a BP), F4

(29,000 to 27,500 cal a BP), F3 (25,300 to 23,800 cal a BP), F2 (22,300 to 19,000 cal a BP) and F1 (17,200 to 15,700 cal a BP) river flood events, already investigated by Martinez-Lamas et al., (2020). HS refers to Heinrich Stadials; YD refers to the Younger Dryas cold event; BA refers to the Bølling-Allerød Interstadial; GS refers to the Greenland Stadials.

3.1.3. The effect of erosion through canyon incisions

Areas with steep slopes, such as those caused by submarine channels present in the Danube deep-sea fan, are more susceptible to slope failure than the surrounding areas (Kvalstad, 2007). Four canyons, including the Viteaz Canyon, SC1, SC2 and SC3 have deeply incised the seafloor along a north-west/south-east direction. With new chronological constraints, we firstly show that the deeper head scarps, which have incised present-day seafloor morphology mostly along the SC1, SC2, SC3 canyon edges **(Fig. 7)**, are older than 33,500 cal BP. Supported by the fact that numerous head scarps are located close to the canyon headwalls and the shelf break, the effect of erosive processes and slope over-steepening should be significant on the initiation of landslides along the upper slope **(Fig. 19)**. The slope value of the canyon flanks locally reaches 25° between 200 m and 900 m water depths, where the axial incision is the most developed (Fig 19 and Riboulot et al., 2017). Local high-inclination values, combined with the erosive flows generated at river mouths when sedimentation rates increase with intensification of river sediment supply (Mulder and Cochonat 1996), could favour the collapse of levees along submarine channels and canyon edges. Deep MTDs mapped in this study (**Fig. 7**) have already been assigned to failure processes (Hillman et al., 2018b), due to the erosive action of turbidity currents during the SC1, SC2 or SC3 canyon activity periods (Marsset et al., 2022). Popescu et al. (2004) suggest retrogressive slides along the western Black Sea submarine canyon edges, induced by successive slope destabilisation on the flanks.

Moreover, Miramontes et al. (2018) demonstrate that in the eastern margin of the Corsica Trough, affected by submarine instabilities, incision at the foot of the slope (canyon incision in our case) highly favours the reduction of shear strength in sedimentary layers along canyon flanks. The authors also indicate that increasing erosion at the foot of the slope induces lateral propagation and lengthening of the shear zone along a specific layer; in our case, SC1, SC2, and SC3 probably acted as active sediment pathways and were associated with increased bottom hyperpycnal current intensities (Martinez-Lamas et al., 2020) during the E-LGP.

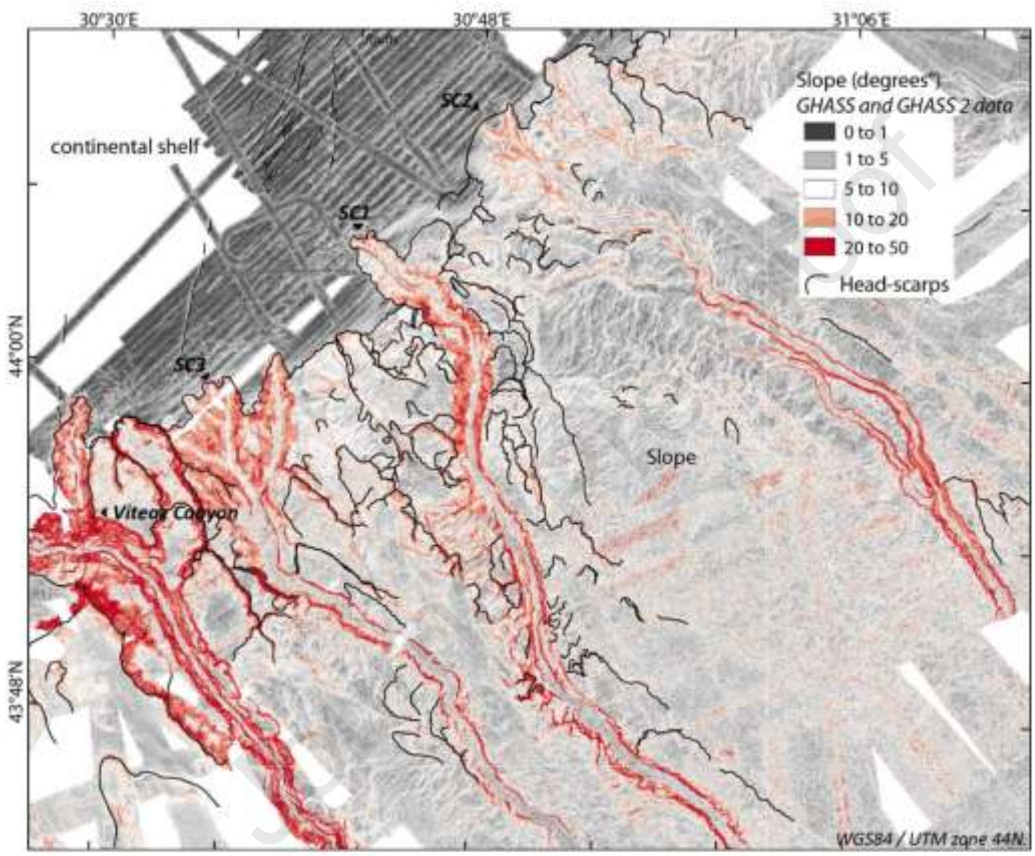

Figure 19: Slope map of the north-western Black Sea margin, highlighting high slope angle along the different canyons incisions. We can note the local high value left by the failure head-scarps. The location of the head-scarps are represented with black lines.

2.3. Triggering factors

3.1.1. The role of gas-hydrate dissociation on slope instability

GH systems are highly sensitive to environmental changes (Kayen and Lee 1991; Dickens 2003; Clennell et al., 1999; Liu and Flemings, 2009; Phrampus and Hornbach, 2012; Ferré et al., 2012; Davies et al., 2021). Recent evolution of Black-Sea pressure-temperature-salinity conditions has been demonstrated to trigger GH decomposition by reducing the GHSZ since the E-LGP (Fabre et al., 2024), and more particularly in response to sea-level variations, temperature warming (Popescu et al., 2006; Pape et al., 2011; Zander et al., 2017; Hillman et al., 2018a; Ker et al., 2019; Colin et al., 2020a), and salinity shifts (Riboulot et al., 2018). Additionally, Riboulot et al. (2018) show that recent salinisation of the Black Sea since the last reconnection with the Mediterranean Sea at -9 ka (Soulet et al., 2011a) has contributed to a major GH dissociation phase, that is still in progress. It is important to notice that salinity values dramatically changed between the fresh-water lake stage and the marine stage basin at -9 ka from 2 psu to 22 psu (Soulet et al., 2011a; Riboulot et al., 2018).

GH dissociation induces the build-up of excess pore pressure that affects in-situ mechanical properties of sediments and therefore promotes slope instability (Kayen and Lee 1991; Dugan and Flemings, 2000; Mienert et al., 2005, Talling et al., 2014; Elger et al., 2018; Liu et al., 2020). Geotechnical experiments, to characterise sediment behaviour in the context of GH decomposition (Sultan et al., 2004 and 2007), show that such a decomposition likely increases permeability in the initial stages. Then, an increase in compressibility induces a build-up in pore pressure at the base of low-permeability layers , thereby accompanying a decrease in-situ shear strength (Wheeler, 1988; Vanoudheusden et al., 2004; Sultan et al., 2004; 2007).

Since the E-LGP, GH dissociation has resulted in the seaward migration of the upper-termination of the GHSZ from its E-LGP position (defined between -33,5 ka and -20 ka), between - 495 m and - 525 m water-depth, to its current position, between -660 m and -725 m water depth (Fabre et al., 2024 and **Fig. 2**). To better understand the possible effects of GH dissociation on slope failure in the area, **Figure 18** shows the estimated age of our failure event in comparison with the evolution of the sea level of the Black Sea since the E-LGP (Constantinescu et al., 2015).

We have thus attempted to compare the zones where successive slides occurred with the predicted paleo and current positions of the GHSZ. During the E-LGP, when low-stand conditions prevailed, the major head scarps initiated on or above the pinch-out of the predicted GHSZ, (**Fig. 20**), except for the three smallest MTDs (~0.5 to 3 km² each) which are associated with failure stage B at -750 m water depth along a regional scarp (**Fig. 14A**). This implies that failure events A and B initiated outside the GHSZ at the E-LGP, on the upper slope where free gas prevailed in bearing sediments **(Fig. 20).** During the sea-level rise period (-15 and -9 ka), failure event C occurred above or between the GHSZ upper limit during the E-LGP and the current one (-660 m) (**Fig. 20**).

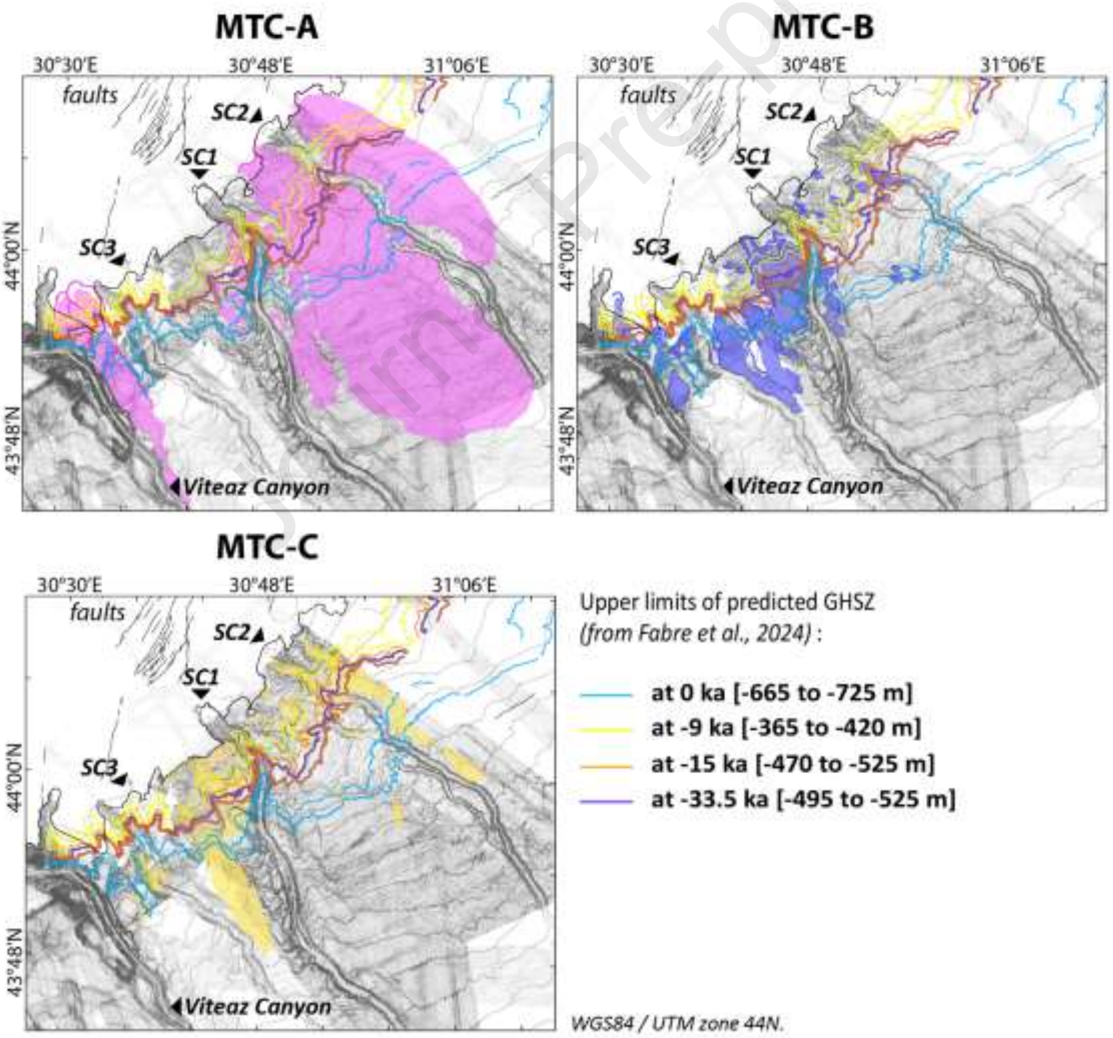

Figure 20: Synthetic representation of the extent of landslides related to failure events A (pink), B (blue), and C (yellow). The upper limits of predicted GHSZ, provided from Fabre et al. (2024) modelling, have been projected

on the bathymetry. The map indicates that excluding isolated landslides located along a regional scarp at ~700 and 800 mbsl, all failure events activated at least above the upper limits of the predicted GHSZ, and inside the GHDZ defined between the E-LGP and the present-day.

Finally, more recently, Fabre et al. (2024) modelled more comprehensively the evolution of the GHSZ from -33.5 ka to present-day in the study area using a dynamic 2D multi-parametric GH stability model developed by Sultan et al. (2010). These results combined with our landslide mapping **(Fig. 21)** show that (1) GH where stable during the E-LGP from -33.5 to -20 ka, i.e. during the initiation of stages A and B, (2) MTC-A and MTC-B mostly initiated in the free-gas domain and when occurring within the GHSZ, are extremely surficial in comparison with the depth of the BGHSZ **(Fig. 21)**. Linking these MTCs to gas-hydrate dissociation is therefore not a convincing possibility. This modelling also shows that MTC-C initiates during a complex period of balancing of the GHSZ associated with the sea-level variations that occurred after -20 ka and the final reconnection of the Black Sea with the Mediterranean at - 9 ka **(Fig. 21).** Consequently, this stage C could be related to GH dissociation phases particularly the most dramatic one related to re-salinisation of the Black Sea. The major uncertainty in the exact timing of this last event prevents any definitive conclusion in terms of cause and effect. MTC-C is the thinnest MTC that we observed, rooted well above the successive modelled BGHSZ **(Fig. 21)**.

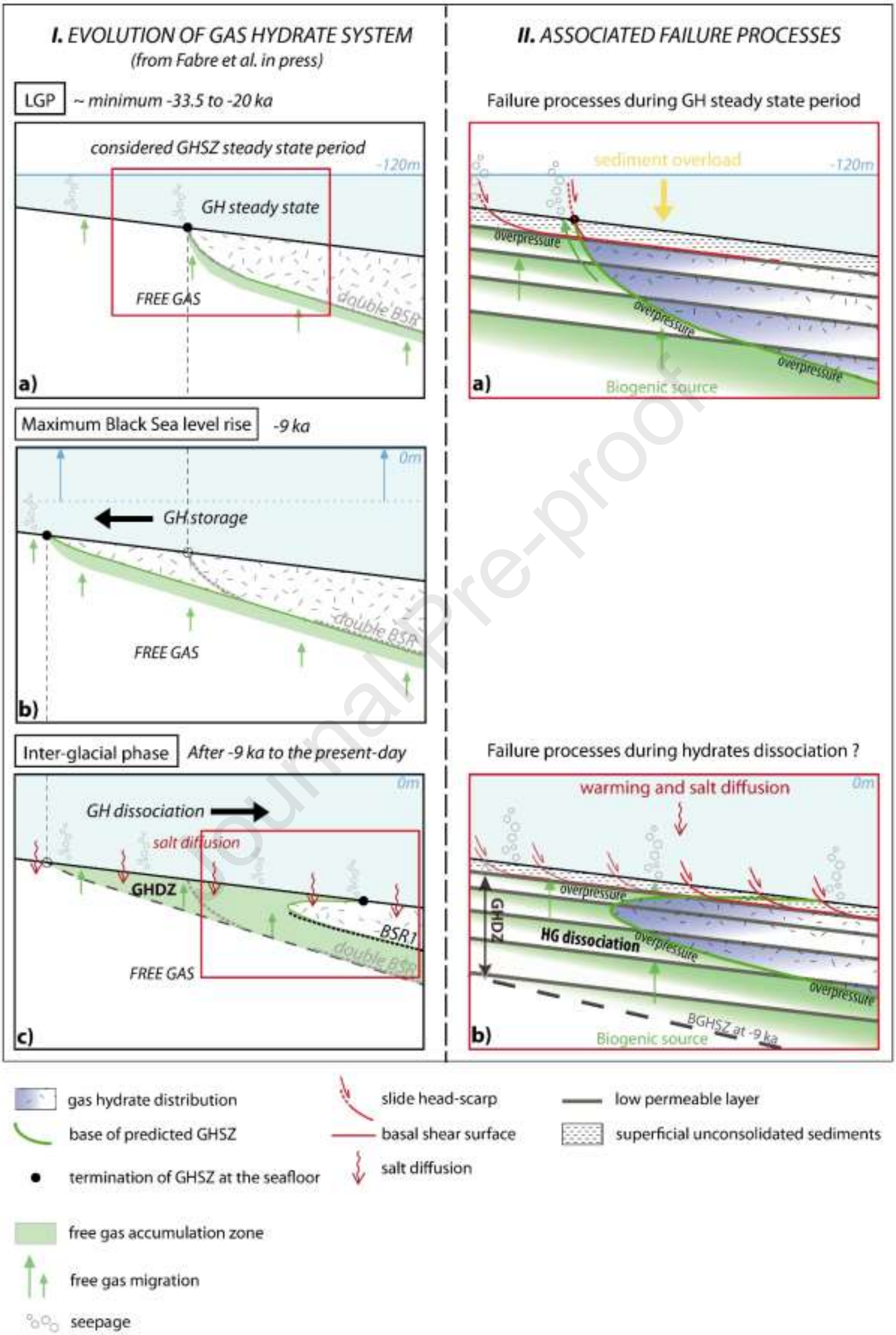
I. EVOLUTION OF GAS HYDRATE SYSTEM
(from Fabre et al. in press)
LGP
~ minimum -33.5 to -20 ka
considered GHSZ steady state period
-120m
GH steady state
FREE GAS
double BSR
a)
Maximum Black Sea level rise
-9 ka
0m
GH storage
FREE GAS
double BSR
b)
Inter-glacial phase
After -9 ka to the present-day
0m
GH dissociation
salt diffusion
GHDZ
BSR1
double BSR
FREE GAS
c)
II. ASSOCIATED FAILURE PROCESSES
Failure processes during GH steady state period
sediment overload
-120m
overpressure
overpressure
overpressure
Biogenic source
a)
Failure processes during hydrates dissociation ?
warming and salt diffusion
0m
overpressure
GHDZ
HG dissociation
overpressure
overpressure
BGHSZ at -9 ka
Biogenic source
b)
gas hydrate distribution
base of predicted GHSZ
termination of GHSZ at the seafloor
free gas accumulation zone
free gas migration
seepage
slide head-scarp
basal shear surface
salt diffusion
low permeable layer
superficial unconsolidated sediments

951

Figure 21: Conceptual model representing the evolution of the GHSZ since the last glacial period given by the position of a double BSR (from Fabre et al., 2024), and proposition of failure mechanisms to explain the failure stages A, B (II.a) and C (II.b).

3.1.2. The effect of free gas

An increase in fluid overpressure in gas-hosting sediments can be a triggering factor of sediment deformations leading to failure initiation (Flemings et al., 2008; Lafuerza et al., 2009, 2012; Plaza-Faverola et al., 2011; Talukder, 2012; Berndt et al., 2012; Riboulot et al., 2013). Excess pore-pressure generation can originate from different external factors, related to: 1) rapid sedimentation especially during low-stand periods when sediment overload can compact gas-hosting sediments; 2) relative sea-level changes, during which the modification of hydrostatic pressure significantly affects the timing and periodicity of gas emissions (Sultan et al., 2020), particularly through the exsolution process which favours gas expulsion from sediments during the stages of sea-level fall. An increase in the gas volumes of fluid reservoirs and the formation of gas bubbles may have induced a local fluid pore-pressure increase and in turn the decrease in effective stress with possible consequences on surficial sediment softening (Lafuerza et al., 2009, 2012; Riboulot et al., 2013, 2019).

As gas exsolution following a drastic sea-level drop may have occurred between -17.2 ka and -15.7 ka (Soulet et al., 2013) **(Fig. 18A)**, it is expected to have played a role in the latest failure stage C. Excess pore-pressure generation must also be considered as a triggering factor for landslides A and B which occurred during an acceleration of sediment accumulation rate (**Fig. 18B and Fig. S1 in Supplementary Material**) particularly on the shelf edge and along canyon flanks during the supposed connection of the Viteaz Canyon with the Danube River.

Lastly, instabilities on canyon flanks may be facilitated by the high content of shallow gas as suggested by Riedel et al. (2021). In the study area, gas emissions are ubiquitous within a sector extending between 200 m and 1000 m water depths and reach a maximum density along the canyon paths **(Fig. 2)**.

3.1.3. Possible tectonic controls

Active tectonics and the release of seismic energy during earthquakes can cause slope instability (e.g. Pope et al., 2017). Based on an earthquake catalogue compilation by USGS (*United States Geological Survey* https://earthquake.usgs.gov/earthquakes/search/), and SHARE (http://www.share-eu.org), we note that some earthquakes occurred in vicinity of the study area during the 1000-2022 period. Lower magnitude earthquakes (M=2.8 to 4) were recorded closer to the shelf break on the Romanian outer shelf at a minimum distance of 20 km from the initiation zones. One event (M=4.4) was recorded in the study area, on the slope domain, at 1400 m water depth, 20 km from the initiation zone. Moderate earthquakes (M=3.7, 4.4 and 4.6) occurred offshore the study area, in the lower slope at a minimum distance of 60 km from the initiation area. Additional higher magnitude events (M=4 to 5.5) were recorded in the western Black Sea, particularly offshore Bulgaria and Ukraine, localised more than 100 km from the study area. Therefore, paleo-seismic activity can be considered as a possible triggering factor for the landslides observed and this could explain the synchronicity of failure during the same event.

Secondly, gravity tectonics have affected the study area. Pre-Oligocene gravity-driven faults described by Dinu et al. (2002, 2005), Tambrea et al. (2000), Konerding et al. (2010), Munteanu et al. (2011), Matenco et al. (2016) and evidenced by new geophysical data acquired during the GHASS-2 cruise (2021), intersect the seafloor. The extension of these faults on the western Black Sea outer shelf is very close to the identified MTD initiation zones (a few kilometres) **(Fig. 2)**. They correspond to a very well-expressed set of SW-NE normal faults clearly visible on bathymetry and affecting recent sediments with vertical offsets in the order of a few metres to tens of metres. Gravity tectonics and associated block re-adjustments and over-steepening have been proposed to control the location of MTDs in many areas (Loncke et al., 2009; Reis et al., 2010; Brothers et al., 2013). In our case, the MTD initiation areas are not strictly located along those faults, some of the landslides are close to faults, but others are much further away. With these considerations alone, it is very difficult to draw conclusions on the role of paleo-seismicity combined with tectonic activity on slope instabilities.

7. CONCLUSION

Analysis of multiresolution geophysical data correlated with a published core-derived model age establish the first high-resolution mapping and dating of Pleistocene-Holocene MTDs that occurred on the upper slope of Romanian Black Sea margin since the E-LGP. This study clearly highlights that, despite robust environmental and slope failure model age since the E-LGP, identifying landslide-controlling factors remains difficult; in many cases, different initiation factors may interact.

Many slope failures occur near the Danube-related canyons, in a domain where gas escapes and GH dissociation are very active, arguing the link between both processes and eventual associated risks. However, our study demonstrates that the response of sediments to gas hydrate decomposition is far from being straightforward.

- We show that the two major failure events occurred during a fresh-water lake low-stand period close to the gas-hydrate occurrence zone but during steady-state GH stability conditions. External factors, such as climate forcing and sea-level fluctuations in the investigated period ranging between the end of the last low-stand period and the beginning of the interglacial period, have led to significant hydrologic implications. During the glacial period, sediment load delivered by the Danube River watershed could have led to slope instability near the shelf edge and particularly for the two most massive failure events (A and B). Canyon incision and slope over steepening along reactivated canyons may also be a local preconditioning factor in generating large MTDs along the north canyons. The effect of free gas could relate to fluid overpressure in transient stratigraphic reservoirs allowing the development of the observed stratigraphic detachment planes.

- The last instability stage age ranges between 15,800 and 8,080 cal BP, a period that underwent severe environmental changes, with a short and abrupt drainage cycle of the Fennoscandian Ice Sheet into the Black Sea watershed (17,200 - 15,700 ± 300 cal a BP), immediately followed by a sea-level drop and a more definitive reconnection and salinisation at -9 ka (Soulet et al., 2011b). Several active combined factors could therefore explain this latest failure event. The most likely being a re-adjustment of the margin, during sea-level variations, implying re-activation of gravity-driven faults or gas exsolution following the rapid sea-level fall, leading to free gas contained in sediments to be expulsed to the seafloor which could have generated softening and destabilisation of very surficial layers. The area affected by hydrate dissociation since the E-LGP is far from the landslide initiation zones.

For all the scenarios cited above, the heterogeneity of the sediment succession is probably also a key preconditioning factor that controls the formation of gas-transient reservoirs in buried sediments. We propose that gas is stored preferentially inside coarse-grained layers with relatively high permeability, explaining the systematic activation of failure events along very surficial and specific layers.

In contrast to many models predicting failure and sliding along the BGHSZ, the correlation of our chrono-stratigraphic study with a recent spatio-temporal dynamic modelling of the evolution of the GHSZ since the E-LGP, shows that the basal shear surfaces of the landslides are very surficial inside and especially outside the GHSZ. The free-gas/hydrate interface did not act as a failure surface. This study allows us to definitively set aside a sudden scenario in the case of gas hydrate dissociation that we might have envisaged for this period of major environmental change and leads us to minimise the *Clathrate gun* hypothesis (Kennett et al., 2003), which argues for a massive gas emission directly into the ocean, and a predisposition of slope sediment instabilities.

8. DATA AVAILABILITY

Data sets used in the current study were acquired during the GHASS (2015) and GHASS-2 expeditions (2021) and data sets are available in the GHASS cruise report (//archimer.ifremer.fr/doc/00300/41141/) (Ker and Riboulot, 2015). They include echosounding and multibeam bathymetry raw data, multi-resolution seismic full raw data (MCS, SBP and SYSIF). Information relative to core GAS-CS01 is also available in open access (//doi.org/10.58006/bfbgx-127384). Three SYSIF profiles are freely available (Colin, Ker and Marsset (2021): //doi.org/10.17882/75247). Seismic data and sub-bottom profiler are available in the following websites repository of GHASS cruise (https://doi.org/10.17600/15000500) and GHASS-2 cruise (https://doi.org/10.17600/18001358) respectively.

9. ACKNOWLEDGEMENTS

The support of the officers and crew during the GHASS (2015) and GHASS-2 (2021) cruises on board R/V Pourquoi pas? was greatly appreciated, as was the dedication of the Genavir and Ifremer technical staff during the cruise. We are grateful to the seismic data processing team Y. Thomas, P. Dupont, E. Thereau, B. Marsset, at the IFREMER Research Institute; We thank N. Sultan for providing insightful comments on fluid migration processes, R. Jatiault, G. Ballas for invaluable discussions at various stages of this work and members of CEFREM laboratory from the University of Perpignan for our multiple scientific discussions. G. Soulet and S. Toucanne are thanked for discussions on the core GAS-CS01 description and model-age information. We also acknowledge A. Chalm for revision of the English language, which greatly helped to improve the manuscript. This work was funded by the BLAME project sponsored by the French National Research Agency (ANR-18-CE01-0007), European programme H2020-DOORS (Project 101000518), IFREMER and the CEFREM laboratory of University of Perpignan Via Domitia.

10.REFERENCES

Aksu, A. E., Hiscott, R. N., Yaşar, D. O. Ğ. A. N., Işler, F. I., & Marsh, S. (2002). Seismic stratigraphy of Late Quaternary deposits from the southwestern Black Sea shelf: evidence for non-catastrophic variations in sea-level during the last~ 10 000 yr. Marine Geology, 190(1-2), 61-94.

Anton, E. M., Munteanu, I., Dinu, C., & Melinte-Dobrinescu, M. C. (2019). Litho-and biostratigraphy of the Eocene deposits from Istria Basin northern edge (Western Black Sea). Geo-Eco-Marina, 25, 55-70.

Badertscher, S., Fleitmann, D., Cheng, H., Edwards, R. L., Göktürk, O. M., Zumbühl, A., ... & Tüysüz, O. (2011). Pleistocene water intrusions from the Mediterranean and Caspian seas into the Black Sea. Nature Geoscience, 4(4), 236-239.

Bahr, A., Lamy, F., Arz, H., Kuhlmann, H., & Wefer, G. (2005). Late glacial to Holocene climate and sedimentation history in the NW Black Sea. Marine Geology, 214(4), 309-322.

Berndt, C., Costa, S., Canals, M., Camerlenghi, A., de Mol, B., & Saunders, M. (2012). Repeated slope failure linked to fluid migration: the Ana submarine landslide complex, Eivissa Channel, Western Mediterranean Sea. Earth and Planetary Science Letters, 319, 65-74.

Bouriak, S., Vanneste, M., & Saoutkine, A. (2000). Inferred gas hydrates and clay diapirs near the Storegga Slide on the southern edge of the Vøring Plateau, offshore Norway. Marine Geology, 163(1-4), 125-148.

Brothers, D. S., Luttrell, K. M., & Chaytor, J. D. (2013). Sea-level–induced seismicity and submarine landslide occurrence. Geology, 41(9), 979-982.

Burwicz, E., & Haeckel, M. (2020). Basin-scale estimates on petroleum components generation in the Western Black Sea basin based on 3-D numerical modelling. Marine and Petroleum Geology, 113, 104122.

Caspers, H. (1957). Black sea and sea of Azov.

Chatterjee, S., Bhatnagar, G., Dugan, B., Dickens, G. R., Chapman, W. G., & Hirasaki, G. J. (2014). The impact of lithologic heterogeneity and focused fluid flow upon gas hydrate distribution in marine sediments. Journal of Geophysical Research: Solid Earth, 119(9), 6705-6732.

Chepalyga, A. L. (1985). Inland sea basins. In: A. A. Velichko (Ed.), Late Quaternary environments of the Soviet Union. University of Minnesota Press, Minneapolis: 229-247.

Clark, P. U., Dyke, A. S., Shakun, J. D., Carlson, A. E., Clark, J., Wohlfarth, B., ... & McCabe, A. M. (2009). The last glacial maximum. *science*, *325*(5941), 710-714.

Clennell, M. B., Hovland, M., Booth, J. S., Henry, P., & Winters, W. J. (1999). Formation of natural gas hydrates in marine sediments: 1. Conceptual model of gas hydrate growth conditioned by host sediment properties. Journal of Geophysical Research: Solid Earth, 104(B10), 22985-23003.

Colin, F., Ker, S., & Marsset, B. (2020a). Fine-scale velocity distribution revealed by datuming of very-high-resolution deep-towed seismic data: Example of a shallow-gas system from the western Black Sea. Geophysics, 85(5), B181-B192.

Colin, F., Ker, S., Riboulot, V., & Sultan, N. (2020b). Irregular BSR: Evidence of an ongoing reequilibrium of a gas hydrate system. Geophysical Research Letters, 47(20), e2020GL089906.

Constantinescu, A. M., Toucanne, S., Dennielou, B., Jorry, S. J., Mulder, T., & Lericolais, G. (2015). Evolution of the Danube deep-sea fan since the last glacial maximum: new insights into Black Sea water-level fluctuations. Marine Geology, 367, 50-68.

Corrick, E. C., Drysdale, R. N., Hellstrom, J. C., Capron, E., Rasmussen, S. O., Zhang, X., ... & Wolff, E. (2020). Synchronous timing of abrupt climate changes during the last glacial period. *Science*, *369*(6506), 963-969.

Davies, R. J., Maqueda, M. Á. M., Li, A., & Ireland, M. (2021). Climatically driven instability of marine methane hydrate along a canyon-incised continental margin. Geology, 49(8), 973-977.

De Leeuw, A., Morton, A., van Baak, C. G., & Vincent, S. J. (2018). Timing of arrival of the Danube to the Black Sea: Provenance of sediments from DSDP site 380/380A. Terra Nova, 30(2), 114-124.

Demaison, G. J., & Moore, G. T. (1980). Anoxic environments and oil source bed genesis. *Organic geochemistry*, *2*(1), 9-31.

Deuser, W. G. (1972). Late-Pleistocene and Holocene history of the Black Sea as indicated by stable-isotope studies. Journal of Geophysical Research, 77(6), 1071-1077.

Dickens, G. R. "A methane trigger for rapid warming?." (2003): 1017-1017.

Dimitrov, L., & Vassilev, A. (2003). Black Sea gas seepage and venting structures and their contribution to atmospheric methane. Annual of the University of Mining and Geology “St. Ivan Rilski”, 46, Part I, Geology and Geophysics, 331-336.

Dinu, C., Wong, H. K., & Tambrea, D. (2002). Stratigraphic and tectonic syntheses of the Romanian Black Sea shelf and correlation with major land structures. Geology and Tectonics of the Romanian Black Sea Shelf and its Hydrocarbon Potential, 2, 101-117.

Dinu, C., Wong, H. K., Tambrea, D., & Matenco, L. (2005). Stratigraphic and structural characteristics of the Romanian Black Sea shelf. Tectonophysics, 410(1-4), 417-435.

Dugan, B., & Flemings, P. B. (2000). Overpressure and fluid flow in the New Jersey continental slope: Implications for slope failure and cold seeps. Science, 289(5477), 288-291.

Dugan, B. (2012). A review of overpressure, flow focusing, and slope failure. In Submarine Mass Movements and Their Consequences: 5th International Symposium (pp. 267-276). Springer Netherlands.

Elger, J., Berndt, C., Rüpke, L., Krastel, S., Gross, F., & Geissler, W. H. (2018). Submarine slope failures due to pipe structure formation. Nature Communications, 9(1), 715.

Fabre, M., Riboulot, V., Loncke, L., Ker, S., Ballas, G., Thomas, Y., ... & Sultan, N. (2024). Slow dynamics of hydrate systems revealed by a double BSR. Geophysical Research Letters, 51(10), e2023GL106284.

Ferré, B., Mienert, J., & Feseker, T. (2012). Ocean temperature variability for the past 60 years on the Norwegian-Svalbard margin influences gas hydrate stability on human time scales. Journal of Geophysical Research: Oceans, 117(C10).

Flemings, P. B., Long, H., Dugan, B., Germaine, J., John, C. M., Behrmann, J. H., ... & Expedition, I. O. D. P. (2008). Pore pressure penetrometers document high overpressure near the seafloor where multiple submarine landslides have occurred on the continental slope, offshore Louisiana, Gulf of Mexico. Earth and Planetary Science Letters, 269(3-4), 309-325.

Haeckel, M., Bialas, J., Klaucke, I., Wallmann, K., Bohrmann, G., & Schwalenberg, K. (2015). Gas hydrate occurrences in the Black Sea–new observations from the German SUGAR project. Fire in the Ice: Methane Hydrate Newsletter, 15(2), 6-9.

Hillman, J. I., Burwicz, E., Zander, T., Bialas, J., Klaucke, I., Feldman, H., ... & Awwiller, D. (2018). Investigating a gas hydrate system in apparent disequilibrium in the Danube Fan, Black Sea. Earth and Planetary Science Letters, 502, 1-11.

Hillman, J. I., Klaucke, I., Bialas, J., Feldman, H., Drexler, T., Awwiller, D., ... & Badhani, S. (2018). Gas migration pathways and slope failures in the Danube Fan, Black Sea. Marine and Petroleum Geology, 92, 1069-1084.

Hiscott, R. N., Aksu, A. E., Mudie, P. J., Marret, F., Abrajano, T., Kaminski, M. A., ... & Yaşar, D. (2007). A gradual drowning of the southwestern Black Sea shelf: evidence for a progressive rather than abrupt Holocene reconnection with the eastern Mediterranean Sea through the Marmara Sea Gateway. Quaternary International, 167, 19-34.

Kayen, R. E., & Lee, H. J. (1991). Pleistocene slope instability of gas hydrate-laden sediment on the Beaufort Sea margin. Marine Georesources & Geotechnology, 10(1-2), 125-141.

Kennett, J. P., Cannariato, K. G., Hendy, I. L., & Behl, R. J. (2003). *Methane hydrates in Quaternary climate change: The clathrate gun hypothesis* (Vol. 54, pp. 1-9). Washington, DC: American Geophysical Union.

Ker, S., Le Gonidec, Y., Marsset, B., Westbrook, G. K., Gibert, D., & Minshull, T. A. (2014). Fine-scale gas distribution in marine sediments assessed from deep-towed seismic data. Geophysical Journal International, 196(3), 1466-1470.

Ker, S., Riboulot, V., & Team, G. C. (2015). GHASS cruise report.

Ker, S., Thomas, Y., Riboulot, V., Sultan, N., Bernard, C., Scalabrin, C., ... & Marsset, B. (2019). Anomalously deep BSR related to a transient state of the gas hydrate system in the western Black Sea. Geochemistry, Geophysics, Geosystems, 20(1), 442-459.

Ketzer, M., Praeg, D., Rodrigues, L. F., Augustin, A., Pivel, M. A., Rahmati-Abkenar, M., ... & Cupertino, J. A. (2020). Gas hydrate dissociation linked to contemporary ocean warming in the southern hemisphere. Nature communications, 11(1), 3788.

Konerding, C. (2005). Mio-Pleistocene sedimentation and structure of the Romanian shelf, northwestern Black Sea (Doctoral dissertation, Staats-und Universitätsbibliothek Hamburg Carl von Ossietzky).

Konerding, C., Dinu, C., & Wong, H. K. (2010). Seismic sequence stratigraphy, structure and subsidence history of the Romanian Black Sea shelf. Geological Society, London, Special Publications, 340(1), 159-180.

Kruglyakova, R. P., Byakov, Y. A., Kruglyakova, M. V., Chalenko, L. A., & Shevtsova, N. T. (2004). Natural oil and gas seeps on the Black Sea floor. *Geo-Marine Letters*, *24*(3), 150-162.

Kvalstad, T. J. (2007, April). What is the current" best practice" in offshore geohazard investigations? A State-of-the-art review. In Offshore technology conference (pp. OTC-18545). OTC.

Kvenvolden, K. A. (1993). Gas hydrates—geological perspective and global change. Reviews of geophysics, 31(2), 173-187.

Kvenvolden, K. A. (1994). Natural gas hydrate occurrence and issues. Annals of the New York Academy of Sciences, 715: 232-246. https://doi.org/10.1111/j.1749-6632.1994.tb38838.x

Kvenvolden, K. (1996). Natural gas hydrate occurrence and issues. *Oceanographic Literature Review*, *5*(43), 468.

Lafuerza, S., Sultan, N., Canals, M., Frigola, J., Berne, S., Jouet, G., ... & Sierro, F. J. (2009). Overpressure within upper continental slope sediments from CPTU data, Gulf of Lion, NW Mediterranean Sea. International Journal of Earth Sciences, 98, 751-768.

Lafuerza, S., Sultan, N., Canals, M., Lastras, G., Cattaneo, A., Frigola, J., ... & Berndt, C. (2012). Failure mechanisms of Ana slide from geotechnical evidence, Eivissa channel, Western Mediterranean Sea. Marine Geology, 307, 1-21.

Lericolais, G., Bulois, C., Gillet, H., & Guichard, F. (2009). High frequency sea level fluctuations recorded in the Black Sea since the LGM. Global and Planetary Change, 66(1-2), 65-75.

Lericolais, G., Guichard, F., Morigi, C., Popescu, I., Bulois, C., Gillet, H., & Ryan, W. B. F. (2011). Assessment of Black Sea water-level fluctuations since the Last Glacial Maximum. Geology and Geoarchaeology of the Black Sea Region: Beyond the Flood Hypothesis, 473, 33.

Lericolais, G., Bourget, J., Popescu, I., Jermannaud, P., Mulder, T., Jorry, S., & Panin, N. (2013). Late Quaternary deep-sea sedimentation in the western Black Sea: New insights from recent coring and seismic data in the deep basin. Global and Planetary Change, 103, 232-247.

Li, A., Davies, R. J., & Mathias, S. (2017). Methane hydrate recycling offshore of Mauritania probably after the last glacial maximum. Marine and Petroleum Geology, 84, 323-331.

Liu, F., Tan, L., Crosta, G., & Huang, Y. (2020). Spatiotemporal destabilization modes of upper continental slopes undergoing hydrate dissociation. Engineering Geology, 264, 105286.

Liu, X., & Flemings, P. (2009). Dynamic response of oceanic hydrates to sea level drop. Geophysical Research Letters, 36(17).

Locat, J., & Lee, H. J. (2002). Submarine landslides: advances and challenges. Canadian Geotechnical Journal, 39(1), 193-212.

Loncke, L., Gaullier, V., Droz, L., Ducassou, E., Migeon, S., & Mascle, J. (2009). Multi-scale slope instabilities along the Nile deep-sea fan, Egyptian margin: a general overview. Marine and Petroleum Geology, 26(5), 633-646.

Major, C., Ryan, W., Lericolais, G., & Hajdas, I. (2002). Constraints on Black Sea outflow to the Sea of Marmara during the last glacial–interglacial transition. Marine Geology, 190(1-2), 19-34.

Marsset, B., Menut, E., Ker, S., Thomas, Y., Regnault, J. P., Leon, P., ... & Sultan, N. (2014). Deep-towed high resolution multichannel seismic imaging. Deep Sea Research Part I: Oceanographic Research Papers, 93, 83-90.

Marsset, B., Ker, S., Thomas, Y., & Colin, F. (2018). Deep-towed high resolution seismic imaging II: Determination of P-wave velocity distribution. Deep Sea Research Part I: Oceanographic Research Papers, 132, 29-36.

Marsset, T., Ballas, G., Munteanu, I., Aiken, C., Ion, G., Pitel-Roudaut, M., & Dupont, P. (2022). Tectonic-sedimentary architecture of surficial deposits along the continental slope offshore Romania (North of the Viteaz Canyon, Western Black Sea): Impact on sediment instabilities. Global and Planetary Change, 208, 103708.

Martinez-Lamas, R., Toucanne, S., Debret, M., Riboulot, V., Deloffre, J., Boissier, A., ... & Soulet, G. (2020). Linking Danube River activity to Alpine Ice-Sheet fluctuations during the last glacial (ca. 33–17 ka BP): Insights into the continental signature of Heinrich Stadials. Quaternary Science Reviews, 229, 106136.

Maslin, M., Owen, M., Betts, R., Day, S., Dunkley Jones, T., & Ridgwell, A. (2010). Gas hydrates: past and future geohazard?. Philosophical Transactions of the Royal Society A: Mathematical, Physical and Engineering Sciences, 368(1919), 2369-2393.

Matenco, L., Munteanu, I., Ter Borgh, M., Stanica, A., Tilita, M., Lericolais, G., ... & Oaie, G. (2016). The interplay between tectonics, sediment dynamics and gateways evolution in the Danube system from the Pannonian Basin to the western Black Sea. Science of the Total Environment, 543, 807-827.

McIver, R. D. (1982). Role of naturally occurring gas hydrates in sediment transport. AAPG bulletin, 66(6), 789-792. https://doi.org/10.1306/03b5a318-16d1-11d7-8645000102c1865d.

Mienert, J., Vanneste, M., Bünz, S., Andreassen, K., Haflidason, H., & Sejrup, H. P. (2005). Ocean warming and gas hydrate stability on the mid-Norwegian margin at the Storegga Slide. Marine and petroleum geology, 22(1-2), 233-244.

Minshull, T. A., Marín-Moreno, H., Betlem, P., Bialas, J., Bünz, S., Burwicz, E., ... & Vázquez, J. T. (2020). Hydrate occurrence in Europe: A review of available evidence. Marine and Petroleum Geology, 111, 735-764.

Miramontes, E., Sultan, N., Garziglia, S., Jouet, G., Pelleter, E., & Cattaneo, A. (2018). Altered volcanic deposits as basal failure surfaces of submarine landslides. Geology, 46(7), 663-666.

Mitchum Jr, R. M., Vail, P. R., & Thompson III, S. (1977). Seismic stratigraphy and global changes of sea level: Part 2. The depositional sequence as a basic unit for stratigraphic analysis: Section 2. Application of seismic reflection configuration to stratigraphic interpretation.

Mountjoy, J. J., Pecher, I., Henrys, S., Crutchley, G., Barnes, P. M., & Plaza-Faverola, A. (2014). Shallow methane hydrate system controls ongoing, downslope sediment transport in a low-velocity active submarine landslide complex, Hikurangi Margin, New Zealand. Geochemistry, Geophysics, Geosystems, 15(11), 4137-4156.

Mulder, T., & Cochonat, P. (1996). Classification of offshore mass movements. Journal of Sedimentary research, 66(1), 43-57.

Mulder, T., Syvitski, J. P., Migeon, S., Faugères, J. C., & Savoye, B. (2003). Marine hyperpycnal flows: initiation, behavior and related deposits. A review. Marine and Petroleum Geology, 20(6-8), 861-882.

Munteanu, I., Matenco, L., Dinu, C., & Cloetingh, S. A. P. L. (2011). Kinematics of back-arc inversion of the Western Black Sea Basin. Tectonics, 30(5).

Naudts, L., Greinert, J., Artemov, Y., Staelens, P., Poort, J., Van Rensbergen, P., & De Batist, M. (2006). Geological and morphological setting of 2778 methane seeps in the Dnepr paleo-delta, northwestern Black Sea. Marine Geology, 227(3-4), 177-199.

Nian, T. K., Song, X. L., Zhao, W., Jiao, H. B., & Guo, X. S. (2020). Submarine slope failure due to overpressure fluid associated with gas hydrate dissociation. *Environmental Geotechnics*, *9*(2), 108-123.

Nikishin, A. M., Korotaev, M. V., Ershov, A. V., & Brunet, M. F. (2003). The Black Sea basin: tectonic history and Neogene–Quaternary rapid subsidence modelling. Sedimentary Geology, 156(1-4), 149-168.

Nisbet, E. G., & Piper, D. J. (1998). Giant submarine landslides. Nature, 392(6674), 329-330.

Nixon, M. F., & Grozic, J. L. (2007). Submarine slope failure due to gas hydrate dissociation: a preliminary quantification. *Canadian Geotechnical Journal*, *44*(3), 314-325.

Özsoy, E., Rank, D., & Salihoglu, I. (2002). Pycnocline and deep mixing in the Black Sea: stable isotope and transient tracer measurements. *Estuarine, Coastal and Shelf Science*, *54*(3), 621-629.

Panin, N. (1989). Danube Delta genesis, evolution and sedimentology. Revue Roumaine de Geologie Geophysique et Geographie: Geographie,, 33.

Panin, N., (1997). Geomorphological zonation of Black Sea. In: V. Mamaev, A. Berlyant, O. Musin et D. Aubrey (Editors), Black Sea Geographic Information System (V 2.0) [CD-ROM]. Black Sea Environmental Programme and UNDP

Panin, N., & Jipa, D. (2002). Danube River sediment input and its interaction with the north-western Black Sea. Estuarine, Coastal and Shelf Science, 54(3), 551-562.

Pape, T., Bahr, A., Klapp, S. A., Abegg, F., & Bohrmann, G. (2011). High-intensity gas seepage causes rafting of shallow gas hydrates in the southeastern Black Sea. Earth and Planetary Science Letters, 307(1-2), 35-46.

Paull, C. K., Buelow, W. J., Ussler III, W., & Borowski, W. S. (1996). Increased continental-margin slumping frequency during sea-level lowstands above gas hydrate–bearing sediments. Geology, 24(2), 143-146.

Pauli, C. K., Ussler, W., & Dillon, W. P. (2003). Potential role of gas hydrate decomposition in generating submarine slope failures. Natural gas hydrate: In oceanic and permafrost environments, 149-156.

Paull, C. K., Dallimore, S., Hughes-Clarke, J., Blasco, S., Lundsten, E., Ussler, W., ... & Collett, T. (2011, May). Tracking the decomposition of submarine permafrost and gas hydrate under the shelf and slope of the Beaufort Sea. In Proceedings of the 7th International Conference on Gas Hydrates (Vol. 1, pp. 1689-1699). Edinburgh, Scotland: ICGH.

Phrampus, B. J., & Hornbach, M. J. (2012). Recent changes to the Gulf Stream causing widespread gas hydrate destabilization. Nature, 490(7421), 527-530.

Plaza-Faverola, A., Bünz, S., & Mienert, J. (2010). Fluid distributions inferred from P-wave velocity and reflection seismic amplitude anomalies beneath the Nyegga pockmark field of the mid-Norwegian margin. Marine and Petroleum Geology, 27(1), 46-60.

Plaza-Faverola, A., Westbrook, G. K., Ker, S., Exley, R. J., Gailler, A., Minshull, T. A., & Broto, K. (2010). Evidence from three-dimensional seismic tomography for a substantial accumulation of gas hydrate in a fluid-escape chimney in the Nyegga pockmark field, offshore Norway. Journal of Geophysical Research: Solid Earth, 115(B8).

Plaza-Faverola, A., Bünz, S., & Mienert, J. (2011). Repeated fluid expulsion through sub-seabed chimneys offshore Norway in response to glacial cycles. Earth and Planetary Science Letters, 305(3-4), 297-308.

Poort, J., Vassilev, A., & Dimitrov, L. (2005). Did postglacial catastrophic flooding trigger massive changes in the Black Sea gas hydrate reservoir?. Terra Nova, 17(2), 135-140.

Pope, E. L., Talling, P. J., & Carter, L. (2017). Which earthquakes trigger damaging submarine mass movements: Insights from a global record of submarine cable breaks?. Marine Geology, 384, 131-146.

Popescu, I., Lericolais, G., Panin, N., Wong, H. K., & Droz, L. (2001). Late Quaternary channel avulsions on the Danube deep-sea fan, Black Sea. Marine Geology, 179(1-2), 25-37.

Popescu, I., Lericolais, G., Panin, N., Normand, A., Dinu, C., & Le Drezen, E. (2004). The Danube submarine canyon (Black Sea): morphology and sedimentary processes. Marine Geology, 206(1-4), 249-265.

Popescu, I., De Batist, M., Lericolais, G., Nouzé, H., Poort, J., Panin, N., ... & Gillet, H. (2006). Multiple bottom-simulating reflections in the Black Sea: potential proxies of past climate conditions. Marine Geology, 227(3-4), 163-176.

Popescu, I., Lericolais, G., Panin, N., De Batist, M., & Gillet, H. (2007). Seismic expression of gas and gas hydrates across the western Black Sea. Geo-Marine Letters, 27, 173-183.

Rank, D., Özsoy, E., & Salihoğlu, İ. (1999). Oxygen-18, deuterium and tritium in the Black Sea and the Sea of Marmara. *Journal of Environmental Radioactivity*, *43*(2), 231-245.

Reis, A. T., Perovano, R., Silva, C. G., Vendeville, B. C., Araujo, E., Gorini, C., & Oliveira, V. (2010). Two-scale gravitational collapse in the Amazon Fan: a coupled system of gravity tectonics and mass-transport processes. Journal of the Geological Society, 167(3), 593-604.

Riboulot, V., Cattaneo, A., Sultan, N., Garziglia, S., Ker, S., Imbert, P., & Voisset, M. (2013). Sea-level change and free gas occurrence influencing a submarine landslide and pockmark formation and distribution in deepwater Nigeria. Earth and Planetary Science Letters, 375, 78-91.

Riboulot, V., Cattaneo, A., Scalabrin, C., Gaillot, A., Jouet, G., Ballas, G., ... & Ker, S. (2017). Control of the geomorphology and gas hydrate extent on widespread gas emissions offshore Romania. Bulletin de la Société géologique de France, 188(4).

Riboulot, V., Ker, S., Sultan, N., Thomas, Y., Marsset, B., Scalabrin, C., ... & Ion, G. (2018). Freshwater lake to salt-water sea causing widespread hydrate dissociation in the Black Sea. Nature communications, 9(1), 117.

Riboulot, V., Imbert, P., Cattaneo, A., & Voisset, M. (2019). Fluid escape features as relevant players in the enhancement of seafloor stability?. Terra Nova, 31(6), 540-548.

Riedel, M., Freudenthal, T., Bergenthal, M., Haeckel, M., Wallmann, K., Spangenberg, E., ... & Bohrmann, G. (2020). Physical properties and core-log seismic integration from drilling at the Danube deep-sea fan, Black Sea. *Marine and Petroleum Geology*, *114*, 104192.

Riedel, M., Hähnel, L., Bialas, J., Bachmann, A. K., Gaide, S., Wintersteller, P., ... & Bohrmann, G. (2021). Controls on gas emission distribution on the continental slope of the western Black Sea. Frontiers in Earth Science, 8, 601254.

Robinson, A. G. (Ed.). (1997). Regional and Petroleum Geology of the Black Sea and Surrounding Region: AAPG Memoir 68 (No. 68). AAPG.

Ross, D. A., & Degens, E. T. (1974). Recent sediments of Black Sea: sediments.

Rowan, M. G., Peel, F. J., & Vendeville, B. C. (2004). Gravity-driven fold belts on passive margins.

Ruppel, C. D., & Kessler, J. D. (2017). The interaction of climate change and methane hydrates. Reviews of Geophysics, 55(1), 126-168.

Ryan, W. B., Pitman III, W. C., Major, C. O., Shimkus, K., Moskalenko, V., Jones, G. A., ... & Yüce, H. (1997). An abrupt drowning of the Black Sea shelf. Marine geology, 138(1-2), 119-126.

Sanchez Goni, M.F., Harrison, S.P., 2010. Millennial-scale climate variability and vegetation changes during the Last Glacial: concepts and terminology. Quat. Sci. Rev. 29, 2823e2827. https://doi.org/10.1016/j.quascirev.2009.11.014

Schnyder, J. S., Eberli, G. P., Kirby, J. T., Shi, F., Tehranirad, B., Mulder, T., ... & Wintersteller, P. (2016). Tsunamis caused by submarine slope failures along western Great Bahama Bank. Scientific reports, 6(1), 35925.

Soulet, G., Delaygue, G., Vallet-Coulomb, C., Böttcher, M. E., Sonzogni, C., Lericolais, G., & Bard, E. (2010). Glacial hydrologic conditions in the Black Sea reconstructed using geochemical pore water profiles. Earth and Planetary Science Letters, 296(1-2), 57-66.

Soulet, G., Ménot, G., Lericolais, G., & Bard, E. (2011a). A revised calendar age for the last reconnection of the Black Sea to the global ocean. Quaternary Science Reviews, 30(9-10), 1019-1026.

Soulet, G., Ménot, G., Garreta, V., Rostek, F., Zaragosi, S., Lericolais, G., & Bard, E. (2011b). Black Sea “Lake” reservoir age evolution since the Last Glacial—Hydrologic and climatic implications. Earth and Planetary Science Letters, 308(1-2), 245-258.

Soulet, G., Ménot, G., Bayon, G., Rostek, F., Ponzevera, E., Toucanne, S., ... & Bard, E. (2013). Abrupt drainage cycles of the Fennoscandian Ice Sheet. Proceedings of the National Academy of Sciences, 110(17), 6682-6687.

Sun, Q., Wu, S., Cartwright, J., & Dong, D. (2012). Shallow gas and focused fluid flow systems in the Pearl River Mouth Basin, northern South China Sea. Marine Geology, 315, 1-14.

Sultan, N., Cochonat, P., Canals, M., Cattaneo, A., Dennielou, B., Haflidason, H., ... & Wilson, C. (2004). Triggering mechanisms of slope instability processes and sediment failures on continental margins: a geotechnical approach. Marine Geology, 213(1-4), 291-321.

Sultan, N. (2007). Comment on Excess pore pressure resulting from methane hydrate dissociation in marine sediments: A theoretical approach by Wenyue Xu and Leonid N. Germanovich-art. no. B02103. *Journal of Geophysical Research*, *112*(B2).

Sultan, N., Voisset, M., Marsset, T., Vernant, A. M., Cauquil, E., Colliat, J. L., & Curinier, V. (2007). Detection of free gas and gas hydrate based on 3D seismic data and cone penetration testing: An example from the Nigerian Continental Slope. Marine geology, 240(1-4), 235-255.

Sultan, N., Plaza-Faverola, A., Vadakkepuliyambatta, S., Buenz, S., & Knies, J. (2020). Impact of tides and sea-level on deep-sea Arctic methane emissions. Nature communications, 11(1), 5087.

Talling, P. J., CLARE, M. L., Urlaub, M., Pope, E., Hunt, J. E., & Watt, S. F. (2014). Large submarine landslides on continental slopes: geohazards, methane release, and climate change. *Oceanography*, *27*(2), 32-45.

Talukder, A. R. (2012). Review of submarine cold seep plumbing systems: leakage to seepage and venting. Terra Nova, 24(4), 255-272.

Tambrea, D., Sindilar, V., & Olaru, R. (2000). The Pontian from the Romanian continental shelf of the Black Sea. Rom. Oil J, 7(1), 9-20.

Tambrea, D., Dinu, C., & Sampetrean, E. (2002). Characteristics of the tectonics and lithostratigraphy of the Black Sea shelf, offshore Romania. Geology and tectonics of the Romanian Black Sea shelf and its hydrocarbon potential. BGF Special Volume, (2), 29-42.

Urlaub, M., Talling, P. J., & Masson, D. G. (2013). Timing and frequency of large submarine landslides: implications for understanding triggers and future geohazard. *Quaternary Science Reviews*, *72*, 63-82.

Vanneste, M., Sultan, N., Garziglia, S., Forsberg, C. F., & L'Heureux, J. S. (2014). Seafloor instabilities and sediment deformation processes: The need for integrated, multi-disciplinary investigations. Marine Geology, 352, 183-214.

Vanoudheusden, E., Sultan, N., & Cochonat, P. (2004). Mechanical behaviour of unsaturated marine sediments: experimental and theoretical approaches. Marine geology, 213(1-4), 323-342.

Vassilev, A., & Dimitrov, L. (2002). Spatial and quantity evaluation of the Black Sea gas hydrates. Russian Geology and Geophysics, 43(7), 672-684.

Vassilev, A., & Dimitrov, L. (2003). Model evaluation of the Black Sea gas hydrates. Comptes Rendus de l'Academie bulgare des Sciences, 56(3), 3-15.

Wang, Y. J., Cheng, H., Edwards, R. L., An, Z. S., Wu, J. Y., Shen, C. C., & Dorale, J. A. (2001). A high-resolution absolute-dated late Pleistocene monsoon record from Hulu Cave, China. Science, 294(5550), 2345-2348.

Wegwerth, A., Kaiser, J., Dellwig, O., Shumilovskikh, L. S., Nowaczyk, N. R., & Arz, H. W. (2016). Northern hemisphere climate control on the environmental dynamics in the glacial Black Sea "Lake". Quaternary Science Reviews, 135, 41-53.

Westbrook, G. K., Thatcher, K. E., Rohling, E. J., Piotrowski, A. M., Pälike, H., Osborne, A. H., ... & Aquilina, A. (2009). Escape of methane gas from the seabed along the West Spitsbergen continental margin. *Geophysical Research Letters, 36*(15).

Wheeler, S. J. (1988). A conceptual model for soils containing large gas bubbles. Geotechnique, 38(3), 389-397.

Winguth, C., Wong, H. K., Panin, N., Dinu, C., Georgescu, P., Ungureanu, G., ... & Podshuveit, V. (2000). Upper Quaternary water level history and sedimentation in the northwestern Black Sea. Marine Geology, 167(1-2), 127-146.

Wong, H. K., Panin, N., Dinu, C., Georgescu, P., & Rahn, C. (1994). Morphology and post-Chaudian (Late Pleistocene) evolution of the submarine Danube fan complex. Terra Nova, 6(5), 502-511.

Yanchilina, A. G., Ryan, W. B., McManus, J. F., Dimitrov, P., Dimitrov, D., Slavova, K., & Filipova-Marinova, M. (2017). Compilation of geophysical, geochronological, and geochemical evidence indicates a rapid Mediterranean-derived submergence of the

Black Sea's shelf and subsequent substantial salinification in the early Holocene. Marine Geology, 383, 14-34.

Zander, T., Haeckel, M., Berndt, C., Chi, W. C., Klaucke, I., Bialas, J., ... & Atgın, O. (2017). On the origin of multiple BSRs in the Danube deep-sea fan, Black Sea. Earth and Planetary Science Letters, 462, 15-25.

Zander, T., Choi, J. C., Vanneste, M., Berndt, C., Dannowski, A., Carlton, B., & Bialas, J. (2018). Potential impacts of gas hydrate exploitation on slope stability in the Danube deep-sea fan, Black Sea. Marine and Petroleum Geology, 92, 1056-1068.

HIGHLIGHTS

- Three surficial failure stages since the end of the last glacial period
- Landslides all initiated in the free-gas domain outside the hydrate zone
- The role of hydrate dissociation on recent failure stages is not suspected
- Fluid overpressure, sediment overload, canyon incision and tectonics are probable factors involved in slope instabilities

Declaration of interests

☐The authors declare that they have no known competing financial interests or personal relationships that could have appeared to influence the work reported in this paper.

☒The authors declare the following financial interests/personal relationships which may be considered as potential competing interests:

Vincent Riboulot reports financial support was provided by French National Research Agency. If there are other authors, they declare that they have no known competing financial interests or personal relationships that could have appeared to influence the work reported in this paper.